

# LOFAR Sparse Image Reconstruction

Hugh Garsden<sup>1</sup>, Julien N. Girard<sup>1</sup>, Jean-Luc Starck<sup>1</sup>, Stéphane Corbel<sup>1</sup>, Cyril Tasse<sup>2,3</sup>, Arnaud Woiselle<sup>1,4</sup>, John P. McKean<sup>5</sup>, and TBD<sup>6</sup>

<sup>1</sup> Laboratoire AIM, UMR CEA-CNRS-Paris 7, Irfu, Service d'Astrophysique, CEA Saclay, F-91191 GIF-SUR-YVETTE CEDEX, France. e-mail: hugh.garsden@cea.fr

<sup>2</sup> SKA South Africa, 3rd Floor, The Park, Park Road, 7405 Pinelands, South Africa

<sup>3</sup> GEPI, Observatoire de Paris, CNRS, Université Paris Diderot, 5 place Jules Janssen, 92190 Meudon, France

<sup>4</sup> Sagem (Safran), 27 rue Leblanc, 75512 Paris Cedex 15, France

<sup>5</sup> Netherlands Institute for Radio Astronomy (ASTRON), Postbus 2, 7990 AA Dwingeloo, The Netherlands

<sup>6</sup> LOFAR builder's list

June 10, 2014

## ABSTRACT

**Context.** The LOFAR Radio Telescope is a giant digital phased array interferometer with multiple antennas gathered in stations placed throughout Europe. As other interferometers, it provides a discrete set of measured Fourier components of the sky brightness. With these samples, recovering the original brightness distribution with aperture synthesis forms an inverse problem that can be solved by different deconvolution and minimization methods.

**Aims.** Recent papers have established a clear link between the discrete nature of radio interferometry measurement and “compressed sensing” theory, which supports sparse recovery methods to reconstruct an image from the measured visibilities. We aimed at the implementation and at the scientific validation of one of these methods.

**Methods.** We evaluated the photometric and resolution performance of sparse recovery method in the framework of the LOFAR instrument on simulated and real data.

**Results.** We have implemented a sparse recovery method in the standard LOFAR imaging tools, allowing us to compare the reconstructed images from both simulated and real data with images obtained from classical methods such as CLEAN or MS-CLEAN.

**Conclusions.** We show that i) sparse recovery performs as well as CLEAN in recovering the flux of point sources, ii) performs much better on extended objects (the root mean square error is divided by a factor up to 10), and iii) provides a solution with an effective angular resolution 2-3 times better than the CLEAN map. Applied to a real LOFAR dataset, the sparse recovery has been validated with the correct photometry and realistic recovered structures of Cygnus A, as compared to other methods. Sparse recovery has been implemented as an image recovery method for the LOFAR Radio Telescope and it can be used for other radio interferometers.

**Key words.** radio interferometry – compressed sensing – numerical methods

## 1. Introduction

Recent years have seen the development and planning of very large radio interferometers such as the LOw Frequency ARray (LOFAR) (van Haarlem et al. 2013) in Europe, and the Square Kilometre Array (SKA) (Dewdney et al. 2009) in Australia and South Africa (through its various precursors and pathfinders).

These new “digital” instruments bring very large sensitivity and Field of View (FoV), as well as tremendous angular, temporal and spectral resolutions in the radio spectrum observable from Earth. In particular, the very low frequency window (in the “VHF” band between  $\sim 10$  and 250 MHz) is being explored (or revisited) with LOFAR, within the scope of various *Key Science Projects*, spanning the search for fast transients search (Stappers et al. 2011) to the study of early cosmology (de Bruyn & LOFAR EoR Key Science Project Team 2012).

### 1.1. The LOFAR instrument

LOFAR is a digital radio interferometer composed of 48 *stations*: 40 constitute the *Core* and *Remote* stations and are distributed in the Netherlands (NL) and 8 *International* stations are

located in Germany, UK, France and Sweden. It has two working bands: the “LBA”-band (*Low-Band Antenna*) from  $\geq 20$  to 80 MHz, and the “HBA”-band (*High-Band Antenna*) from 110 to 250 MHz, lying on either-side of the FM band. One station consists of two arrays composed of fixed crossed dipole antennas, each offering a large FoV (therefore low directivity) and broadband properties<sup>1</sup>. They measure induced electric signals that undergo pre-processing operations in the station back-end, consisting of digitization, interference mitigation, filtering, phasing and summing. All these steps constitute the *beamforming* step of the *phased* antenna array. The output signal of one station is thus similar to that of a synthetic antenna where the beam is *electronically* pointed (rather than mechanically) in the direction of interest. Since most steps are done in the digital side, “multi-beam” observations are possible and are only limited by the electronic hardware (i.e. in FPGAs, by making trade-offs between the observed bandwidth and the number of numerical beams pointing at the sky).

At the interferometer level, the signal from every station is combined in a central correlator in the NL which performs a

<sup>1</sup> see details at [www.lofar.org](http://www.lofar.org)

phased sum or inter-station cross-correlation. The latter operation enables LOFAR to build up as a digital interferometer which samples a wide range of baselines (from  $\sim 70$  m up to  $\sim 1300$  km). The high flexibility of the instrument comes with the necessity of using advanced calibration strategies depending on the type of observations and its expected final sensitivity.

Since late 2012, LOFAR has been opened to the astronomical community via a regular public call for observations<sup>2</sup>. Early results with LOFAR demonstrated the capability of reaching a very high Dynamic Range (DR) on a wide FoV (i.e. several tens of degrees, see for example Yatawatta et al. (2013)), as well as very high angular resolution (Shulevski 2010) at low frequencies.

The systematic wide field survey of the sky facilitates the building of a new catalog of radiosources at low frequencies, providing new calibrators covering all the northern sky (McKean et al. 2010; Heald & LOFAR Collaboration 2013). As a consequence, powerful known radio sources (including the main calibrators used in radio interferometry) that were unresolved below  $\sim 300$  MHz are now resolved by the LOFAR baselines, making the calibration task more complex to handle. However, LOFAR will improve our understanding of the morphology of the sources as well as processes of emission occurring at lower energies (e.g. de Gasperin et al. (2012)). In addition to increased angular resolution, greater time and frequency resolution can lead to the discovery of predicted sources (Epoch of Reionization signal, exoplanets...) and new sources (e.g. pulsars, the Unknown...) at various angular and time scales.

### 1.2. Increased complexity of low frequency imaging

Since the beginning of radio interferometry, various imaging methods have been designed to fit the requirements of different kinds of (extended) radio objects. The availability of high-performance computing, and the need for efficient, fast and accurate imaging for new wide-field interferometers, has motivated the implementation of new imaging algorithms. Given the recording time/frequency resolutions, the integration time, and the diversity of baselines of wide-field interferometers, large amounts of data storage are required to save the telescope data. These data must then be transformed into a scientifically exploitable form (typically into images cubes). Substantial computational power is also required for this (Begeman et al. 2011).

Because of the nature and the dimensions of the LOFAR array, *Direction-Dependent Effects* (DDE) (Tasse et al. 2012) occur during the span of a LOFAR observation, and add up to the usual other effects intervening in classical radio interferometers. These effects require a “direction-dependent” calibration before imaging. In particular, the classical compact planar array (lying under the same portion of the fluctuating local ionosphere) & small FoV assumptions are no longer valid, especially for a wide-field instrument such as LOFAR.

The problem can be generalized and expressed in the *Measurement Equation* framework (see §2.5). The calibration problem therefore manifests as an inverse problem that should be solved in order to determine independently all the parameters and coefficients that describe each observed dataset.

Among the recent developments of data processing/reconstruction algorithms, the “discovery” of Compressed Sensing (CS) (Candès et al. 2006) has led to new approaches to the solving of these problems. It has been proposed for radio interferometry (e.g. Wenger et al. (2010); Li et al. (2011a,b)) as

the latter constitutes a relevant practical case due to the sparse nature of the interferometric sampling (§2.4).

The implementation of sparse radio image reconstruction methods is expected to produce better results on large extended objects with high angular resolution, compared to other classical deconvolution methods. In §2, we will first present the application of the theory of sparse reconstruction within the scope of radio aperture synthesis imaging, followed by its implementation in the LOFAR imaging software, and we will relate it to prior CLEAN-based deconvolution methods. We then present in §3, the results of benchmark tests using simulated and real LOFAR datasets by focusing on the quality of the image reconstruction compared to that of usual CLEAN-based algorithms. We then discuss the practical advantages and limitations of the current implementation and possible future developments.

## 2. Image reconstruction: from CLEAN to Compressed Sensing

### 2.1. Introduction

An ideal radio interferometer, composed of co-planar and identical antennas, samples the sky in the Fourier domain (Wilson et al. 2009). In other words, each pair of antennas, forming one baseline, give access to the measure of the sky brightness as seen through a set of fringes which has characteristics that depend on the frequency, the baseline length, and orientation with respect to the source. As for optical interferometers, the measured quantity (after correlation of the pair of signals) is the fringe contrast, also called (fringe) *visibility*. In the radio domain where the electric field is slowly varying, we can sample both phase and amplitude with time and frequency. In the scope of radio interferometry, the measured visibility is a complex quantity named the complex visibility.

For an ideal interferometer composed of  $N$  antennas, all  $N(N-1)/2$  independent visibility measurements contribute to sample the complex visibility function which is associated with the Fourier representation of the sky brightness. We define the spatial frequency coordinates system  $(u,v)$ , as the projected baseline on a plane orthogonal to the direction of observation (the third coordinate,  $w$ , is omitted in the small field approximation). This direction defines the origin of the Fourier conjugated coordinate system on the sky, the “direction cosines”  $(l,m)$ .

At any given time and frequency, one baseline samples one spatial frequency of the sky brightness and is represented by one point in the  $(u,v)$  plane of the complex visibility function. If the telescope observes over a long period of time, the projection of the interferometer with respect to the source will vary and will enrich the visibility plane with new samples. A given baseline will “sweep” out a path in the  $(u,v)$  plane (an effect also called *Earth rotation synthesis*). Figure 1 presents the  $(u,v)$  coverage of one typical LOFAR observation integrated over 6 hours. The tracks show the set of  $(u,v)$  samples that are recorded during the observation. The shape of the tracks depends on the interferometer configuration, its latitude and the direction of observation.

The number of visibilities recorded by the interferometer is usually small, because of the limited number of baselines, and the limited observed bandwidth leading to a sparsely populated Fourier space. This collection of samples is the starting point for the process of imaging, which consists of using the measured information to approach the “true” visibility function in the Fourier domain. An image can be generated by gridding the visibilities to a 2D approximation of the Fourier transform and by back-projecting this approximation to the image plane. Due

<sup>2</sup> see the observation proposal section on [www.astron.nl](http://www.astron.nl)

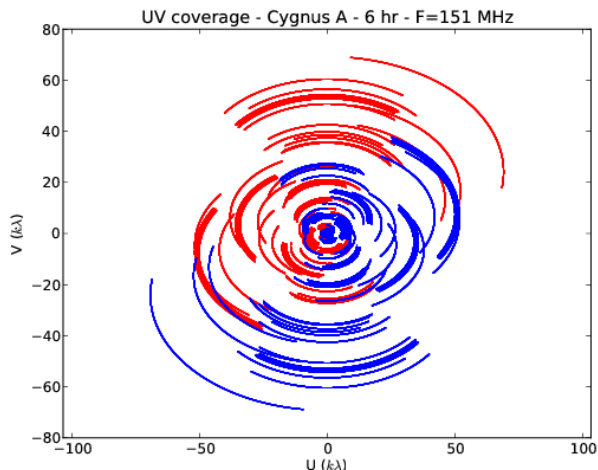


**Fig. 1.** Visibility coverage from a 6-hour observation of Cygnus A (McKean et al. 2010). Visibilities are plotted in the Fourier space with the  $U$  ( $x$  axis) and  $V$  ( $y$  axis) being the spatial frequencies in wavelength unit,  $\lambda$  (here  $f=151$  MHz,  $\lambda \approx 2$  m) determined by the baseline projection on the sky. Each  $(u,v)$  points (red) has its symmetric  $(-u,-v)$  point (blue) corresponding to the same baseline. The lines indicate  $(u,v)$  points where a visibility was recorded. The arcs are built from the variation of the baseline projection with the rotation of the Earth during the observation.

to the missing samples of the visibility function, the image is qualified as *dirty*, and is a rough approximation of the sky brightness. This dirty image is the convolution of the *true* sky brightness (represented as a 2D image) with the interferometer point spread function (PSF). The back-projection of the PSF forms the interferometer *dirty* beam.

One of the most famous methods used to recover the true sky brightness, is the CLEAN method (Högbom 1974) and its derivatives.

We will now discuss the different approaches that can be used to retrieve the sky brightness from the measured visibilities, starting with the CLEAN method, before describing the method based on the sparsity of the measured signal.

## 2.2. CLEAN

For many years, deconvolution has been achieved through the CLEAN algorithm (Högbom 1974) and its variants (Clark 1980; Schwab 1984). CLEAN considers the dirty image to be constructed from point sources convolved with the PSF; extended objects will be decomposed as point sources as closely as possible. CLEAN operates in the direct space of the dirty image (original versions like Högbom do), by locating the maximum of the image and iteratively subtracting a fraction of the dirty beam centered and scaled to the located maximum. The detected sources are indexed as *CLEAN components* to form a *model* image enriched by the successive subtraction steps. The source detection and subtraction continues until a threshold is reached on the dirty image (typically representing the background level). The resulting image forms the *residual* image. The model image contains the pixel description of the locations and the levels of the detected CLEAN components. The model image cannot be used as it is as it doesn't correspond, in the classical interferometric approach, to real structures. In order to remove those unphysical high spatial frequencies components (associated with

the pixel size) that are introduced by the CLEAN algorithm, the model image is usually smoothed to provide a final angular resolution corresponding to that accessible by the interferometer. The final image is formed by convoluting the model image with this smooth function usually taken as the elliptical Gaussian 2D fit of the center of the dirty beam, the *CLEAN beam*. The residual image, which represents the noisy “sky background”, theoretically containing no more detectable radio sources, is added to the convolved CLEAN image to form the *restored* image.

This image can be described in the following manner:

$$I = M * C + \mathcal{R} \quad (1)$$

where  $I$  is the restored image,  $M$  is the model composed of CLEAN component,  $C$  is the CLEAN beam,  $\mathcal{R}$  is the residual, and  $*$  is the convolution operator.

The CLEAN method has several variants, one of which is Cotton-Schwab CLEAN (CoSch-CLEAN), which was used for all experiments in this article (Schwab 1984). The running cycle is conceptually split into major and minor cycles; the minor cycle does a fast examination of the image using only a portion of the dirty beam (assuming a fairly smooth dirty beam with low sidelobes), selects points for PSF removal and perform an Högbom CLEAN in the image plane. The major cycle takes the list of CLEAN components indexed so far, projects them in the Fourier plane and subtracts them from the visibility data (and not from the *gridded* Fourier data, as in Clark CLEAN). This limits the propagation of errors due to the data gridding and of aliasing and enhance the convergence to the real sky image.

With LOFAR, the PSF varies over the field of view, and is also difficult to determine accurately due to instrumental DDEs (§2.5). Moreover, the sensitivity and the variety of baseline brought by the instrument often limit the quality of the restored images using these methods.

## 2.3. Toward Multiresolution

The CLEAN method is well known to produce poor solutions when the image contains large-scale structures. Wakker & Schwarz (1988) introduced the concept of Multiresolution Clean (M-CLEAN) in order to alleviate difficulties occurring in CLEAN for extended sources. The M-CLEAN approach consists of building two intermediate images, the first one (called the smooth map) by smoothing the data to a lower resolution with a Gaussian function, and the second one (called the difference map) by subtracting the smoothed image from the original data. Both images are then processed separately. By using a standard CLEAN algorithm on them, the smoothed clean map and difference clean map are obtained. The recombination of these two maps gives the clean map at the full resolution.

This algorithm may be viewed as an artificial recipe, but it has been shown that it is linked to wavelet analysis (Starck & Bijaoui 1991), leading to a Wavelet CLEAN (W-CLEAN) method (Starck et al. 1994). Furthermore, in the W-CLEAN algorithm, the final solution was derived using a least-square iterative reconstruction algorithm applied to the set of wavelet coefficients detected by applying CLEAN on different wavelet scales. This can be interpreted as a debiasing post-processing of the peak amplitudes found at the different scales. A positivity constraint on the wavelet coefficients was imposed during this iterative scheme by nullifying the negative coefficients.

Another multiscale approach, the Multi-Scale CLEAN (MS-CLEAN) (Cornwell 2008), consists of fitting a collection of extended patches (or blobs). Instead of subtracting the dirty beam

at a given location of the residual at each iteration, as in the CLEAN algorithm, MS-CLEAN subtracts a blob, estimating first which blob size is the most adequate. MS-CLEAN presents however several problems that do not exist in M-CLEAN or W-CLEAN. Indeed, it is unclear which function the algorithm minimizes, or even if it minimizes something at all. The varying background is also problematic in MS-CLEAN (as in CLEAN), while it is not in W-CLEAN. MS-CLEAN also relies on an arbitrary setting of the scales of the image.

However, these different CLEAN-based algorithms (hereafter denoted  $x$ -CLEAN) have all shown to improve significantly the results over CLEAN when the image contains extended sources.

#### 2.4. Compressed Sensing and Sparse Recovery

Compressed Sensing (CS) (Candès et al. 2006; Donoho 2006) is a sampling/compression theory based on the sparsity of an observed signal, which shows that, under certain conditions, one can exactly recover a  $k$ -sparse signal (a signal for which only  $k$  pixels have values different from zero, out of  $n$  total pixels, where  $k < n$ ) from  $m < n$  measurements. CS requires the data to be acquired through a random acquisition system, which is not the case in general. However, even if the CS theorem does not apply from a rigorous mathematical point of view, some links can still be considered between real life applications and CS. In astronomy, CS has already been studied in many applications such as data transfer from satellites to earth (Bobin et al. 2008; Barbey et al. 2011), 3D weak lensing (Leonard et al. 2012), next generation spectroscopic instrument design (Ramos et al. 2011) and especially aperture synthesis. Indeed, the close relation between CS principles and the aperture synthesis image reconstruction problem was first addressed in Wiaux et al. (2009); Wenger et al. (2010); Li et al. (2011c); wide-field observations were subsequently studied in McEwen & Wiaux (2011), and different antennae configurations were analyzed in a compressed sensing framework in Fannjiang (2013). Aperture synthesis presents the three major ingredients that are fundamental in CS:

- **Underdetermined problem:** we have less measurements (i.e. visibilities), than unknowns (i.e. pixel values of the reconstructed image).
- **Sparsity** of the signal: the signal to reconstruct can be represented with a small number of coefficients (that quickly tend to zero when ordered in decreasing power). For point source observations, the solution is even strictly sparse (in the Dirac domain) since it is composed only of a list of spikes. For extended objects, sparsity can be obtained in another representation space such as wavelets.
- **Incoherence** between the acquisition domain (i.e. Fourier domain) and the domain of sparsity. Point sources, for instance, are localized in the pixel domain, but spread over a large domain of the visibility plane. Conversely, each visibility contains information about all sources in the FoV.

From the CS perspective, the best way to reconstruct an image  $X$  from its visibilities is to use sparse recovery, by solving the following optimization problem:

$$\min_{\alpha} \|X\|_p \quad \text{subject to} \quad \|V - AX\|_2^2 < \epsilon, \quad (2)$$

where  $V$  is the measured visibilities vector,  $A$  the operator that embodies the realistic acquisition of the sky brightness components (instrumental effects, DDE...), and  $\|z\|_p^p = \sum_i |z_i|^p$ . To reinforce the sparsity the solution,  $p$  must be less or equal to

1. In particular, for  $p = 0$ , we get the  $\ell_0$  pseudo-norm which counts the number of non-zero entries in  $z$ . The first term enforces sparsity and the second term indicates that the reconstruction matches the visibilities within some error  $\epsilon$ .

Most natural signals, however, are not exactly sparse but rather concentrated within a small set. Such signals are termed *compressible* or *weakly sparse*, in the sense that the sorted pixel values decay quickly according to a power law. The faster the amplitude of pixel values decay, the more compressible the signal is.

It is interesting to note that the CLEAN algorithm can be interpreted as a *Matching Pursuit algorithm* (Lannes et al. 1997) which minimizes the  $\ell_0$  pseudo-norm of the sparse recovery problem of Eq. 2, but recent progress in the field of numerical optimization (see Carrillo et al. (2013) and references therein) allows us to have much faster algorithms. The sparsity model is extremely accurate for a field containing point sources, since the true sky can in this case be represented just by a list of spikes. This explains the very good performance of Högbom CLEAN for point sources recovery, and why astronomers still use it 40 years after it has been published. But CS provides a context in which we can understand the limitation of CLEAN for extended object reconstructions. Indeed, extended objects are not sparse in the pixel basis, and therefore sparse recovery algorithms cannot provide good solutions in this basis. Representing the data in another domain where the solution is sparse, i.e. wavelets in Wakker & Schwarz (1988); Starck et al. (1994), was shown to be a good approach. More generally, we can assume the solution  $X$  can be represented as the linear expansion

$$X = \Phi\alpha = \sum_{i=1}^t \phi_i \alpha_i, \quad (3)$$

where  $\alpha$  are the synthesis coefficients of  $X$ ,  $\Phi = (\phi_1, \dots, \phi_t)$  is the dictionary whose columns are  $t$  elementary waveforms  $\phi_i$  also called *atoms*. The dictionary  $\Phi$  is a  $b \times t$  matrix whose columns are the normalized atoms, supposed here to be normalized to a unit  $\ell_2$ -norm, i.e.  $\forall i \in [1, t], \|\phi_i\|_2^2 = \sum_{n=1}^n |\phi_i[n]|^2 = 1$ . The minimization problem of Eq. 2 can now be reformulated in two ways, the synthesis framework

$$\min_{\alpha} \|\alpha\|_p \quad \text{subject to} \quad \|V - A\Phi\alpha\|_2^2 < \epsilon, \quad (4)$$

and the analysis framework

$$\min_{\alpha} \|\Phi^t X\|_p \quad \text{subject to} \quad \|V - AX\|_2^2 < \epsilon. \quad (5)$$

When the matrix  $\Phi$  is orthogonal, both analysis and synthesis frameworks lead to the same solution.

A signal can be decomposed in many dictionaries, but the best one is the one which provides the sparsest (i.e. the most economical) representation of the signal. In practice, it is convenient to use dictionaries with fast implicit transforms (such as the wavelet transforms, curvelet transforms, etc.) which allow us to directly obtain the coefficients and reconstruct the signal from these coefficients using fast algorithms running in linear or almost linear time (unlike matrix-vector multiplications).

#### 2.5. Imaging with LOFAR

For a large multi-element digital interferometer such as LOFAR observing in a wide FoV, the small field approximation is no longer valid, and the sampled data (represented by the operator  $A$ ) is no longer a discrete set of 2D Fourier components of the

sky. The instrumental and “natural” direction-dependent effects have to be taken into account for proper image reconstruction. These effects include:

- the instrumental effects such as inter-station clock shifts.
- the non-coplanar nature of the baselines (Cornwell & Perley 1992) (the sample visibility function has a non-zero third coordinate, i.e.  $w \neq 0$ ).
- the anisotropic directivity of the phased array beam (Bhatnagar et al. 2008a), and the non-trivial dipole projection effects with time and frequency.
- the sparsity in the sampling of the visibility function (i.e. the limited number of baselines and the time/freq integration).
- the effect of the interstellar- and interplanetary media, and Earth’s ionosphere, on the incoming plane waves.

These effects can be modeled in the framework of the Radio Interferometry Measurement Equation (RIME, see Hamaker et al. (1996); Sault et al. (1996) and following papers) which describes the relation between the sky and the 4-polarization visibilities associated with each pair of antennas in a time-frequency bin. It can model all the DDE mentioned above, cumulated in  $2 \times 2$  Jones matrices that influence the electric field and voltages measurements. One of the most basic ways to express a 4-polarization visibility of one baseline using the RIME formalism is as follows (in a given time-frequency bin) :

$$V_{pq}^{\text{real}} = J_p^{-1} \cdot V_{pq}^{\text{mes}} (J_q^H)^{-1} \quad (6)$$

with

- $V^{\text{mes}}$  the four-polarization (XX,XY,YX,YY) measurement matrix corrupted by the DDE.
- $V^{\text{true}}$  the true visibility matrix uncorrupted by the DDE.
- $J_p$  the cumulated Jones matrices of antenna p
- $J_q^H$  the Hermitian transpose (conjugated transpose) of antenna q

The corrected visibilities  $V_{pq}^{\text{corr}}$  matrix can be expressed as a four-dimensional vector (which also depend on the time  $t$  and frequency  $\nu$ ) as follows (Tasse et al. (2013), Eq. 1) :

$$\text{Vec}(V_{pq}^{\text{corr}}) = \int_S (D_{q,s}^{\nu,*} \otimes D_{p,s}^{\nu}). \text{Vec}(I_s) \times e^{-2i\pi\phi(u,v,w,s)} ds \quad (7)$$

where  $I$  is the four-polarization sky,  $s$  the pointing direction,  $\otimes$  the Kronecker product producing a  $4 \times 4$  matrix (referred to as the Mueller matrix),  $\text{Vec}()$  the operator that transforms a  $2 \times 2$  matrix into a four-dimensional vector,  $D_{q,s}^{\nu,*} \otimes D_{p,s}^{\nu}$ , the  $4 \times 4$  “Mueller” matrix, containing the accumulation of the direction-dependent terms and the array geometry (see details in Appendix A in Tasse et al. (2013)), and  $\phi(u, v, w, s) = ul + vm + w(\sqrt{1 - l^2 - m^2} - 1)$ , the baseline and direction-dependent phase factor.

Because the sky is described in terms of stokes intensity (I, Q, U, V), and not in terms of the electric field value, the RIME is linear in its sky-term. By considering the total set of visibilities over baselines, time and frequency bins, and by including the measurement noise  $\epsilon$ , we can therefore reduce Eq. 7 to:

$$V = A \cdot I + \epsilon \quad (8)$$

with

- I the four-polarization sky
- A the transformation matrix from the sky to the visibilities, including all DDE.
- $\epsilon$  the measurement noise

The structure of the matrix  $A$  and its connection to the RIME and Jones formalism shown above is described in detail in Tasse et al. (2012). The linear operator  $A$  contains (i) the Fourier kernels, as well as the information on (ii) the time-frequency-baseline dependence of the effective  $2 \times 2$  Jones matrices, and (iii) the array configuration which is reduced in that case to be the (u,v,w)-sampling over time and frequency. It is important to note that both (ii) and (iii) cause  $A$  to be non-unitary, which is a very important fact for the work presented in this paper. In practice, it is virtually impossible to make  $A$  explicit, essentially because of its  $N_{\text{vis}} \times N_{\text{pixels}}$  dimension. Instead,  $A$  and  $A^H$  can be applied to any sky or visibility vector respectively using A-projection (Bhatnagar et al. 2008b; Tasse et al. 2013).

To cope with the non-coplanar effect, the  $W$ -projection algorithm (Cornwell et al. 2008) is used to turn the 3-D recorded visibilities into a 2-D Fourier transform.

In the scope of the LOFAR project and its data reduction pipeline, the  $AW$ imager (Tasse et al. 2013) program was developed for imaging the LOFAR data by taking into account both A- and W-projections. It is therefore of high interest to implement CS in a new generation imager.

## 2.6. Algorithm

To perform the sparse image reconstruction, we need to:

1. Select a minimization method to solve Eq. 4 or Eq. 5:
2. Select a dictionary.
3. Select the parameter related to the minimization method.

Several minimization methods have been used for aperture synthesis, the FISTA method (Fast Iterative Shrinkage-Thresholding Algorithm) (Beck & Teboulle 2009)) in Li et al. (2011c); Wenger et al. (2010); Hardy (2013); Wenger et al. (2013), OMP (Orthogonal Matching Pursuit) (G.Davis et al. 1997) in Fannjiang (2013), or SDMM (Simultaneous-Direction Method of Multipliers, Combettes & Pesquet (2011) in Carrillo et al. (2013). In our experiments, we have investigated mainly two algorithms, FISTA and a recent algorithm proposed by Vü (2013) which works in the analysis framework. As both were providing very similar results, we have chosen to report in this paper results derived with the FISTA algorithm. Full details can be found in Beck & Teboulle (2009), Wenger et al. (2010) and Starck et al. (2010).

The choice of dictionary is critical. Optimal dictionaries should contain atoms which represent well the content of the data. In this sense, the starlet transform, also called isotropic undecimated wavelet transform (Starck et al. 2010) that was used in Li et al. (2011c), is a very good choice, since this decomposition has shown to be extremely useful for astronomical image restoration (Starck & Murtagh 2006). On the contrary, orthogonal or bi-orthogonal wavelets, even using several decompositions, are well known to produce artifacts due to critical sampling. Other dictionaries such as curvelets (Starck et al. 2010) are a good alternative if the data contains directional features, such as jets, which will be poorly represented with wavelets. The Block Discrete Cosine Transform (BDCT), used in Fannjiang (2013), is relatively hard to justify for astronomical images, since its atoms present an oscillatory pattern. In this study, we will therefore use two kind of dictionaries, starlet and curvelets.

The final problem remains the choice of the parameters that is needed to control the algorithm. Most minimization methods, using  $l_0$  and  $l_1$ , have a thresholding step, where coefficients in the dictionary have to be soft or hard-thresholded using a threshold value  $\lambda$  (see Starck et al. (2010) for more details on hard

and soft thresholding). This parameter controls the trade-off between the fidelity to the observed visibility and the sparsity of the reconstructed solution. In Li et al. (2011c) and Wenger et al. (2013),  $\lambda$  was fixed to an arbitrary value, different for each experiment, and certainly after several tests. This approach may be problematic for real data where the true solution is not known. In Carrillo et al. (2013),  $\lambda$  is estimated from an arbitrary value  $\beta$ , fixed to  $10^{-3}$ , multiplied to  $\|\Phi_t A^t y\|_\infty$ . The threshold is therefore a fraction of the maximum of the coefficients obtained by decomposition of the dirty map in the chosen dictionary. For a pixel basis, this would result in suppressing everything which is below  $\beta$  times the maximum of the dirty map. We propose in this paper another strategy, where the threshold is fixed only from the noise distribution. This has two main advantages, i) the default threshold value should always give reasonable results, and ii) it optimizes the probability detection of faint objects. Indeed, an arbitrary threshold value could lead to many false detections in the case where the value is too small, and on the contrary many objects may be missed when the value is too large. At the  $n^{\text{th}}$  iteration of the FISTA algorithm, the residual  $R^n$  is calculated by :

$$R^n = \mu A^t (V - A\Phi\alpha^n) \quad (9)$$

where  $V$  are the measured visibilities,  $\alpha^n$  are the coefficients in the dictionary  $\Phi$  of the solution at the  $n^{\text{th}}$  iteration, and  $\mu$  is the FISTA relaxation parameter which depends on the matrix  $F = A\Phi$  ( $\mu$  must verify  $0 < \mu < \frac{1}{\|F\|}$ ). The noise level can then be estimated using a robust estimator such as the MAD (Median of the Absolute Deviation):

$$\sigma = \frac{MAD(R^n)}{0.6745} \quad (10)$$

and the threshold  $\lambda$  is derived by  $\lambda = k\sigma$ , where the parameter  $k$  fixes the probabilities of false detections. The scale factor in Eq. 10 is derived from the quantile function of a normal distribution taken at probability 3/4 (see Tukey et al. (2000)). If the chosen dictionary is the wavelet or the curvelet transform, then the noise level can even be estimated for each band  $j$  of the decomposition. This provides the advantage of handling properly correlated noise. Denoting  $\alpha^{(R)} = \{\alpha_1^{(R)}, \alpha_2^{(R)}, \dots, \alpha_j^{(R)}\}$  as the coefficients of  $R$  in the dictionary  $\Phi$ , the noise level  $\sigma_j$  in each band  $j$  is

$$\sigma_j = \frac{MAD(\alpha_j^{(R)})}{0.6745}, \quad (11)$$

and the threshold is now different for each band,  $\lambda_j = k\sigma_j$ .

### 3. Benchmarking of the sparse recovery

#### 3.1. Benchmark data preparation

The performance of CS can be determined and compared to that of other imaging methods such as Cotton-Schwab CLEAN (CoSch-CLEAN) and MS-CLEAN. We used here three different LOFAR datasets (Table 3.1) for comparing CS and CLEAN-based algorithms in simulated and real situations.

We implemented CS by creating a new method in *AWimager* based on the current CoSch-CLEAN implementation. This new method serves as an entry point to the LOFAR imager for connecting an external library (developed by the authors, see §5.2). This library includes dictionaries (wavelets and curvelets), transforms and minimization methods described above. The CS cycle involves a continual passing of data back and forth between

*AWimager* and the library (for *AWimager* to perform the *gridding*, the *degridding* from the visibility data to the Fourier plane and also perform the A- and W-projections). At each step in the CS cycle, *AWimager* performs the following operations:

- takes as input a new image reconstruction previously obtained (represented in the selected dictionary) from the library
- simulates the visibilities using the same  $A$  operator as for CoSch-CLEAN
- compares the simulated visibilities to the original ones
- passes the difference back to the dictionary, which performs the CS minimization and thresholding step, and produces a reconstructed image.

The process stops if the maximum number of iterations is reached or if a convergence criterion (based on the noise of the residual) is met. *AWimager* outputs a similar set of files for the CLEAN-based algorithms and for CS. Among them, the reconstructed (or *restored*) image, a residual image, a model image and a PSF image. The recovered CLEANed image is the model image (containing CLEAN components) convolved with the CLEAN beam (which is the Gaussian fit of the *dirty* beam; the instrumental PSF) plus the residuals. In the case of CS, the restored image is the solution  $\Phi\alpha^n$  (Eq. 9). The program user may choose to convolve the compressed sensing output with the CLEAN beam or not (see discussion in §4.1). The output model image of CS (directly in Jy/pixel) can be converted to a brightness map (in Jy/beam) for comparison to the other reconstructed images, by multiplying the pixel values by the CLEAN beam area.

The CS residual is an image representation of  $R^n$  (Eq. 9) at the last iteration of compressed sensing and is analogous to the residual at the output of CLEAN (Högbom 1974). Another image can be generated – the error image – which is the difference between the original simulated image (when available) and the CLEAN and compressed sensing recovered images.

By selecting the CS method, the meaning of some classical imager parameters are changed in the scope of the previous definitions: the *gain* is classically used in CLEAN as the fraction of the PSF level used to subtract from a peak location in the dirty image. In CS, the gain is the relaxation parameter  $\mu$  of Eq. 9. The *threshold* value in CLEAN-based methods is a flux density value associated to the level of noise measured (or expected) in the residuals (or in an empty patch of the dirty map). One usually set this level to  $n$  times the noise of an empty patch of the dirty image. Setting this threshold to zero will basically lead x-CLEAN to false detections of sources from the features lying in the background noise. As discussed above in §2.6, the thresholding parameter has a specific meaning in the scope of CS and one should not confuse it with the flux density threshold of x-CLEAN.

The number of iterations for a CLEAN-based algorithm is set to a large value (basically an unlimited number of iterations) so that they will stop when the flux density threshold is reached. The number of iterations for CS can be specified to an arbitrary value or be controlled by a convergence criterion.

The following numerical quantities were taken as figures of merit to measure the quality of the reconstruction using CS and CLEAN-based methods:

- the total flux density computed in a region  $S$  around the source
- the residual image standard deviation (Std-dev) and root mean square (r.m.s.) computed over the same region of the

Name	A	B	C
Sources	Two point sources	Source grid & W50	Cygnus A
Nature of the data	Simulated	Simulated	Real
Pointing RA (hms)	02h45m00.0"	14h11m20.9s	19h59m28.0s
Pointing DEC (dms)	+52°54m54.4s	+52°13m55.2s	+40°44m02.0s
Station configuration	CS	CS+RS	CS+RS
$N_{\text{stations}}$	48	55	36
$N_{\text{correlations}}$	1176	1540	666
$UV_{\text{max}}$ (k $\lambda$ )	3.7 k $\lambda$	~65 k $\lambda$	~39 k $\lambda$
Maximum resolution	~1'	~3"	~5"
Polarization		(linear) XX, YY, XY, YX	
$t_{\text{start}}$ (UT)	6-Nov-2013/00:00:00.5	13-Apr-2012/18:25:05.0	2-Mar-2013/05:50:50.0
$t_{\text{end}}$ (UT)	6-Nov-2013/00:59:59.5	14-Apr-2012/04:44:56.6	2-Mar-2013/11:50:40.0
$\delta t$ (s)	1	10.01	10.01
$N_{\text{times}}$	3600 (=1 Hr)	37192 (~10 Hrs)	21590 (~6 Hrs)
$\nu_0$ (MHz)	150.1	116.2	151.2
$\Delta\nu$ (MHz)	0.195	0.183	0.195
Section	§3.2.1	§3.2.2 & §3.3.1	§3.3.2

**Table 1.** Summary information of the considered LOFAR datasets for the present study. Here, CS stands for *Core Stations* and RS for *Remote Stations*.  $N_{\text{stations}}$  and  $N_{\text{correlations}}$  are respectively the number of stations and the corresponding number of independent correlation measurements (computed as  $N_{\text{correlations}} = N_{\text{stations}}(N_{\text{stations}} - 1)/2 + N_{\text{stations}}$ ). Autocorrelations were systematically flagged before imaging.  $UV_{\text{max}}$  is the largest radial distance in the (u,v) plane which limits the maximum theoretical resolution of the instrument. Start and end observation times are in Universal Time (UT), providing a total number of time samples  $N_{\text{times}}$  at a time resolution  $\delta t$ . For the two first datasets, we considered only one sub-band (SB) of one channel covering a bandwidth  $\Delta\nu$  centered around the frequency  $\nu_0$ . All three datasets come in *Measurements Sets* that follow the NRAO standards. The **A** dataset has been generated for a 1-hour synthetic zenith observation using *mkant* and *makeMS* routines that are part of the LOFAR software package. The **B** dataset comes from a LOFAR commissioning observation and is filled with simulated data. The **C** dataset contains actual calibrated data from a real LOFAR Observation of Cygnus A.

input source object in the residual map or over the full map **I**.

- the error image and the Mean Square Error (MSE) computed over **I** when a model image is available.
- the dynamic range (DR) defined as the ratio of the maximum of the image to the residual Std-dev.

The present paper is composed of different applications that are presented in an order corresponding to the increase complexity of the imaged source. In §3.2, we consider the reconstruction of unresolved point sources in two typical situations implied by new generation radio interferometers: at low angular scale, we investigate the high resolution properties (*super resolution*) of the CS reconstruction by imaging two points sources separated by a varying angle and in different noise regimes (§3.2.1); at a larger scale, we test the robustness of the CS reconstruction when applied to high-dynamic and wide-field imaging using a grid of point sources (§3.2.2). In §3.3, we monitor the quality of the CS reconstruction with datasets containing extended emissions: from a simulated W50 observation (§3.3.1) and a real LOFAR observation of Cygnus A (§3.3.2). A summary of the studies is compiled in §3.4.

## 3.2. Unresolved sources

### 3.2.1. Angular separation between two sources

When considering point sources, the CLEAN-based algorithms are the most used deconvolution methods in radio interferometry. The first test that must be satisfied for a new imaging method, such as CS, is to successfully perform the reconstruction of relatively simple sources with known flux densities. When the sources are point sources, CLEAN-based algorithms are strong competitors for CS whose performances should at least match that of the standard CLEAN method.

In the context of LOFAR, we have generated empty datasets describing a simulated 1-hour observation using a subset of

LOFAR stations. We restrained the full LOFAR array to only *core* stations, which are almost always included in every LOFAR observation. It is therefore of interest to measure the theoretical performances of CS when only this subset is used. The layout of the core stations is slightly elongated (~10%, van Haarlem et al. (2013)) in the North-South direction, providing a symmetric beam pattern to a direction different (but close) to zenith. In this dataset, we pointed the array to the zenith, which will induce a slightly non-symmetrical beam pattern.

As depicted in the table 3.1, the *core* stations provide an approximate maximum resolution of 1' at  $\nu_0=150$  MHz (in the HBA band). During the imaging process, we restricted the (u,v) coverage to the radial distances  $[r_{(u,v)}^{\text{min}}, r_{(u,v)}^{\text{max}}] = [0.1 \text{ k}\lambda, 1.6 \text{ k}\lambda]$  to artificially impose an angular resolution of ~2'.

We “filled” the empty datasets with simulated data using *BBS* (*Blackboard Self-cal*, the standard LOFAR calibration tool described in Pandey et al. (2009)) which predicts the contribution of all sources listed in a given input *sky model* to the complex visibility measurements of every baselines of a given observation. Using the restriction on the Fourier plane mentioned above, we prepared the same dataset to benchmark CLEAN deconvolution and CS reconstruction.

We simulated two 1-Jansky point sources at frequency  $\nu_0$ . One source is located at the phase center and the second one is located at varying angular distances  $\delta\theta$  ranging from 10" up to 5' (in order to cross the instrumental angular resolution of ~2.8', deduced from the PSF). Given our dataset, these values span over three different regimes where the performances of CLEAN and CS are compared: i) sources are unresolved, ii) partially resolved or iii) fully resolved. As we are close to the phase center, the effects mentioned in §2.5 are either corrected or negligible (which will no longer be the case in §3.2.2). The compatibility of CS with the DDE correction provided by *AWimager* is addressed in §3.2.2. For the different angular separation values, we injected Gaussian noise in the complex data to obtain SNR levels

of  $\sim 3$ ,  $\sim 9$ ,  $\sim 16$  in the image. We also considered the *noise-free* case where no supplementary noise was injected. In this case,  $\text{SNR} \approx 2000$  and the noise originates from the background residuals due to the poor sampling of the visibility function. In a more realistic case, the noise depends on the time and frequency integration and, at each station, on the station sensitivity through the SEFD (*System Equivalent Flux Density*). As we want to restrict the number of free parameters and as we only use *core* LOFAR stations, we have not considered this fine modeling of the instrumental noise for this experiment.

We used the CoSch-CLEAN and CS imaging methods implemented in *AWimager*, which serves here as the common testing environment for this study (the A and W projections are not critical here as the two sources are near the phase center). We performed 10000 iterations for the CoSch-CLEAN and 200 iterations for CS. As different levels of noise will be simulated, we set the  $k$  parameter (Eq. 11) to 3 times the noise. We used, in both cases, the full observation, truncated in the (u,v) plane as described above, and we produced  $512 \times 512$  pixel images with  $5''$  pixel resolution using the natural weighting scheme for both algorithms to improve the SNR of the resulting images.

The figure 2 illustrates the results of CS reconstruction (left column), the distribution of CLEAN components in the model image with CoSch-CLEAN (middle column) and the corresponding restored image with CoSch-CLEAN, using the CLEAN beam as the convolution function. We represented the images obtained with the noise-free datasets. The rows correspond to seven typical values of angular separation  $\delta\theta$  from  $30''$  to  $3'$  by steps of  $30''$  except for the  $\delta\theta = 1'15''$  case. There is no *model* image, in the sense of CLEAN, for the CS reconstruction, as the output of CS is directly the best representation of the true sky at a finite resolution (similar to the comparison of models in Li et al. (2011c)). Different angular separation criteria can be chosen. One can look at the final CLEAN model image to see if two identical Fourier components (separated by at least 1 pixel) were detected during the CLEAN maximum search in the residuals. It is also possible to use the Rayleigh criterion in the image plane or source finders (see below).

Here (and hereafter), the CLEAN beam, setting the highest angular resolution of CLEAN deconvolved images, has a size of  $3.18' \times 2.55'$  (major  $\times$  minor axes) as depicted by the shape of unresolved individual point sources on the convolved CLEAN images.

In the CoSch-CLEAN model image, when  $\delta\theta$  increases, only one CLEAN component is detected at a position shifted toward the mean position of the two sources. Starting from  $\delta\theta = 1'30''$ , additional CLEAN components are being detected on the *wings* of the main component. With  $\delta\theta$  increasing, the amplitude of these side CLEAN components increase and contribute to form an elongated shape on the convoluted CLEAN image. Starting from  $\delta\theta = 2'30''$ , the two sources are correctly separated as two distinct groups of pixels located on average around the true position of the source. The position uncertainty of these two sources is still high ( $\sim 30''$ ). For larger separations than  $\delta\theta = 3'$ , the astrometric and flux density errors start to decrease. In the regime where CoSch-CLEAN can not resolve unambiguously the two sources, the features present in the model images (the central components as well as the wing components) can not be associated to real sources. In the scope of this method, an exploitable image with limited resolution, can only be obtained after convolution with the CLEAN beam.

With CS, we directly obtain the best estimate of the sky, as shown on the reconstructed image in the left column of Fig. 2. In the partially resolved regime, we also notice the elongation

of the source size leading to a shift of its position occurring at  $\delta\theta = 1'$ . We note that the two point sources are then resolved at lower angular separation ( $\delta\theta \sim 1'15''$ ) than for CoSch-CLEAN. An elliptical fitting of the FWHM of the sources gives the source size which can be seen as the effective CS convolution beam. In this case, its dimensions are of  $1.55' \times 1.09'$ , representing a beam of cross-section approximately  $1.39'$ , smaller than that of the CLEAN beam. In addition to the improved angular separability, the CS constructed sources are also correctly located in the image (e.g. the fixed source lies close to the vertical mark on Fig. 2 for  $\delta\theta \leq 1'30''$ ) as compared to the CoSch-CLEAN model image, where the CLEAN components are only correctly positioned starting from  $\delta\theta \leq 2'30''$ . In the noise-free case, by using exactly the same dataset and imaging parameters, these results suggest that CS is able to recover information on the true sky beyond the theoretical resolution limit (that is constant in this dataset).

Because there is always a non-zero level of noise in the calibrated interferometric data, we tested the robustness of this characteristic against the image SNR by using the different noisy datasets mentioned above. To compute the effective angular separability of the sources using CoSch-CLEAN and CS, we have used the LOFAR pyBDSM<sup>3</sup> package (*python Blob Detection and Source Measurement*) which consists of island detection, fitting and characterization of all structures in the image. We defined a detection threshold so that no other artifact could be detected as source in the images, as we are only focusing on the two simulated point sources. We used the same set of detection parameters for both methods CoSch-CLEAN and CS.

At a specific SNR level, the value of angular separation at which two distinct components can be detected by the source finders, gives an estimate of the separability angle of the sources, and therefore, the effective resolution that limits the typical size of genuine physical features. The CoSch-CLEAN beam and the effective CS beam are not circular, therefore, the effective angular resolution may depend on the orientation of these beams with respect to the direction joining the two sources. To have a measure that is independent of this direction, it is probably better to compute the ratio of the effective resolution produced by CoSch-CLEAN to that produced by CS.

Using an appropriate sampling of  $\delta\theta$  and noise levels, we can build a graph of this effective resolution deduced from the separability of the two sources for different SNR levels. On Fig. 3 are presented the resulting curves obtained with CoSch-CLEAN (black) and CS (red). At each SNR, we can derive the effective improvement brought by CS by noting the angle  $\delta\theta_{min}$  at which the two sources are separated.

On the one hand, we can see that the CoSch-CLEAN separability has a limited dependence on the SNR, which makes it a stable and robust algorithm for detecting point sources in various SNR regimes. On other hand, CS has a different behavior. At a high SNR regime, the separability values outperforms that of CoSch-CLEAN by a factor of 2–3 in the [10,2000] range. When the SNR decreases, the separability of CS tends to that of CoSch-CLEAN.

In terms of astrometric error, the detected point source locations can be compared to the  $(\alpha, \delta)$  coordinates of the input sky model. The relative position errors do not exceed  $1'$  for CS and  $3'$  for CLEAN for all the different noise levels.

In addition to the angular separability and astrometric error, the flux density of the source has been inspected. We integrated the flux density in the image (either on the reconstructed/model

<sup>3</sup> See <http://www.lofar.org/wiki/doku.php> for more information.

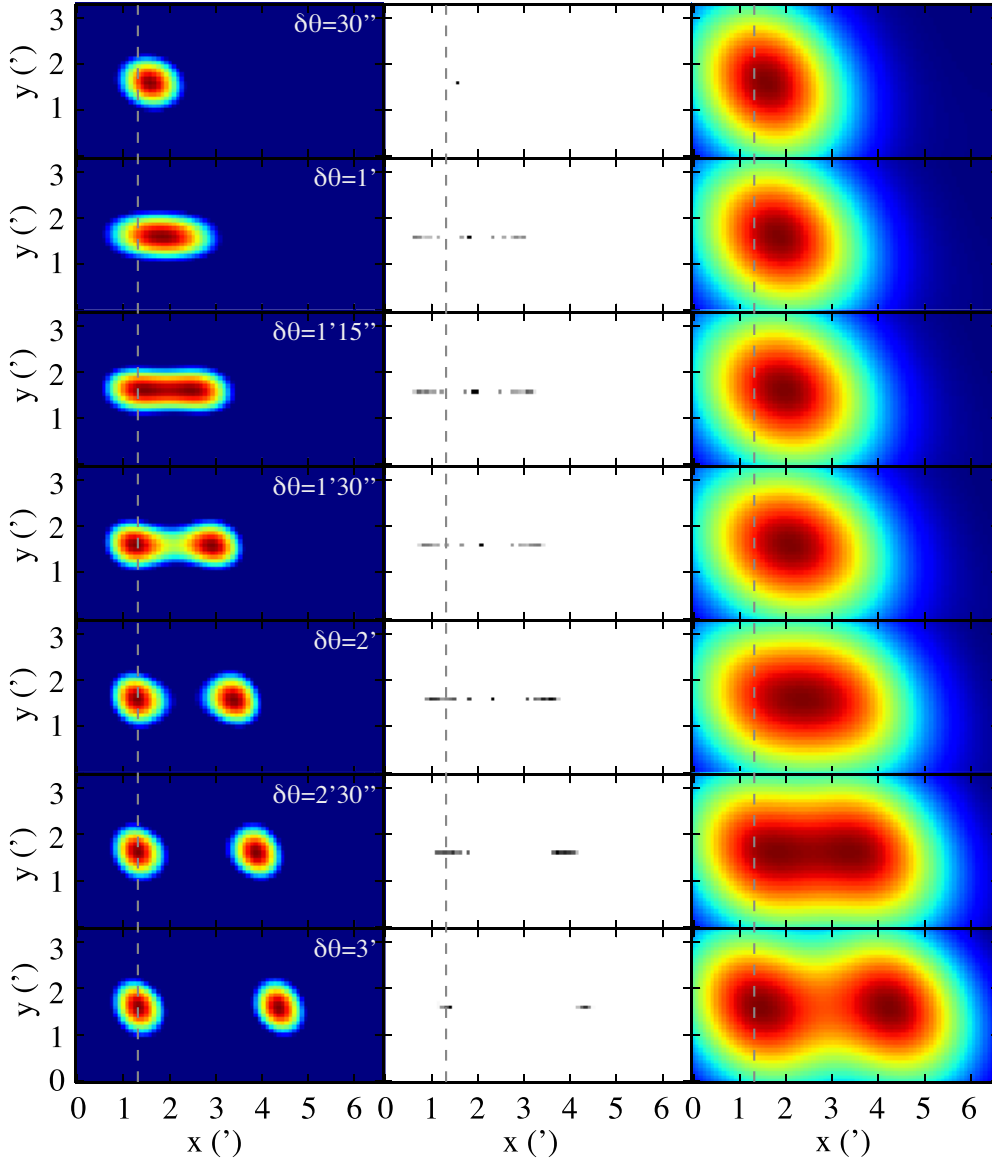


**Fig. 2.** Resulting reconstructed CS image (left column), CoSch-CLEAN model (middle column) and convolved (right column) images obtained from a simulation of different point sources with angular separation  $\delta\theta$  from  $30''$  to  $3'$  by steps of  $30''$  (from top to bottom) except for  $\delta\theta=1'15''$ . The third column was obtained by convolving the CLEAN components (middle column) with the CLEAN beam of FWHM  $3.18' \times 2.55'$ . The two sources recovered separation, after imaging by the different methods, occurs at smaller angular separation with CS (between  $\delta\theta=1'$  and  $\delta\theta=1'15''$ ) than with CoSch-CLEAN (between  $\delta\theta=2'$  and  $\delta\theta=2'30''$ ). The location of the two sources was recovered to within few pixel errors, starting from  $\delta\theta=1'30''$  for CS and  $\delta\theta=3'$  for CoSch-CLEAN. Each cropped image was originally of size  $512 \times 512$  pixels of  $5''$ . The  $(u,v)$  coverage has been restricted to the domain  $[0.1 \text{ k}\lambda, 1.6 \text{ k}\lambda]$  to enforce an artificial resolution of  $\sim 2''$ . The color map scales are normalized to the maximum of each image and they were not represented for clarity. The contrast of the CLEAN components (middle columns) was enhanced to ease their visibility. The grey vertical dash line marks the true position of the source located at the phase center of the dataset.

image, in units of Jy/pixel, or in the convolved image in units of Jy/beam, knowing the CoSch-CLEAN beam area) in a region around the source and compared it to the sky model. Because we have used 1 Jy sources we can directly derive the flux density error from the measures. Naturally, the flux density error of the reconstructed sources is affected by the level of the background noise and scale with the SNR. For CS, it is found to be 3% in the low noise regime and up to 25% in the high noise regime, and respectively, 3% to 23% for CoSch-CLEAN.

From this perspective, it appears that CS provides results that are almost as good results as CLEAN, by default, and provides an improved angular separability with high and moderate SNR data. Compared to the CLEAN model image, where no source can be separated below the PSF size, the structures that are im-

aged with CS can still be trusted in terms of astrometric accuracy and integrated photometry. Regarding the reconstruction of single point sources, CS has demonstrated better performance than CoSch-CLEAN at high and moderate SNR regimes, and has similar performance in a low SNR regime. The low astrometric and flux density error confirm the super resolution capability of CS, which suggests the possibility of dramatically improved angular resolution of extended emission from poorly sampled interferometric data.

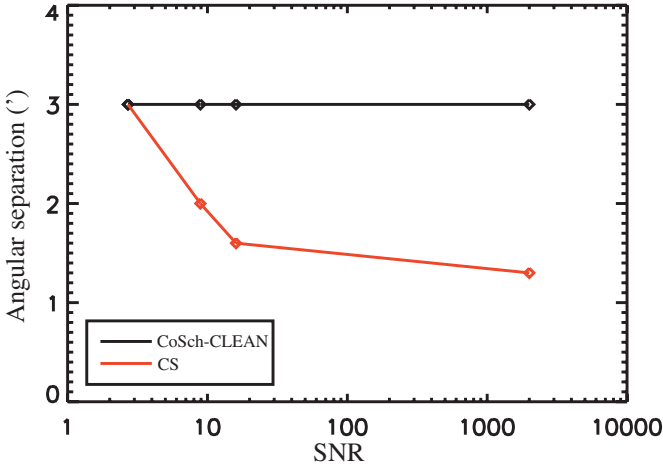


**Fig. 3.** Values of  $\delta\theta_{min}$  of source separability as a function of the SNR, for CS (red curve) and CoSch-CLEAN (black curve). In the moderate (SNR  $\geq 5$ ) and high SNR regimes, the resulting source separability is respectively improved by a factor 1.3 to  $\lesssim 2$ .

### 3.2.2. Wide-field imaging of a grid of sources

We now focus on another aspect of radio imaging at low frequency, namely the wide-field imaging of the sky containing a distribution of point sources of different flux densities. The LOFAR interferometer is composed of stations, each being equivalent to a mechanically pointed antenna toward the direction of interest. These antennas provide a significant FoV which allow the whole LOFAR array to image wide fields inside the *station analog beam*. Inside the LOFAR correlator, one can perform sub-pointing of the array by trading bandwidth with the number of *digital beams*.

As most sources observed by a radiotelescope appear as unresolved point sources in a wide-field image, it is important to verify that CS recovers correctly the flux density of sources that are away from the phase center. *AWimager* is the tool that computes the A operator, enabling to perform this wide-field imaging efficiently (Tasse et al. 2013). This operator A, as defined in the RIME framework, must be compatible with a sparse reconstruction approach.

In this case we simulated 100 point sources arranged on a square grid covering a region of  $8^\circ \times 8^\circ$  around the phase center. The simulated source flux densities values ranged from 1 to 10000 Jy.

We used dataset **B** as a synthetic observation to receive the simulated visibilities. In BBS, we included the simulation of the beam (for the A-projection). The W-projection only depends on the layout of the interferometer which is already included in the dataset.

Noise was injected into the dataset so that it had an RMS value of  $10^{-4}$  (so  $\sim 1$  Jy) relative to the peak of the dirty image.

The points are at equidistant vertices in the grid so as not to interfere on the restored image. The image allows us to examine the distribution of the flux density and the potential distortion over the map. While this arrangement is unrealistic, we can still monitor the astrometric and flux density accuracy versus radial distance from the phase center. We applied CoSch-CLEAN and CS to the simulated dataset containing the grid. The model image for the point sources appears a set of pixels and is not shown; the dirty image generated from visibilities is shown in Fig. 4.

We used  $1024 \times 1024$  pixel images with a pixel size of  $28''$  and the entire (u,v) coverage of the dataset **B** was included in

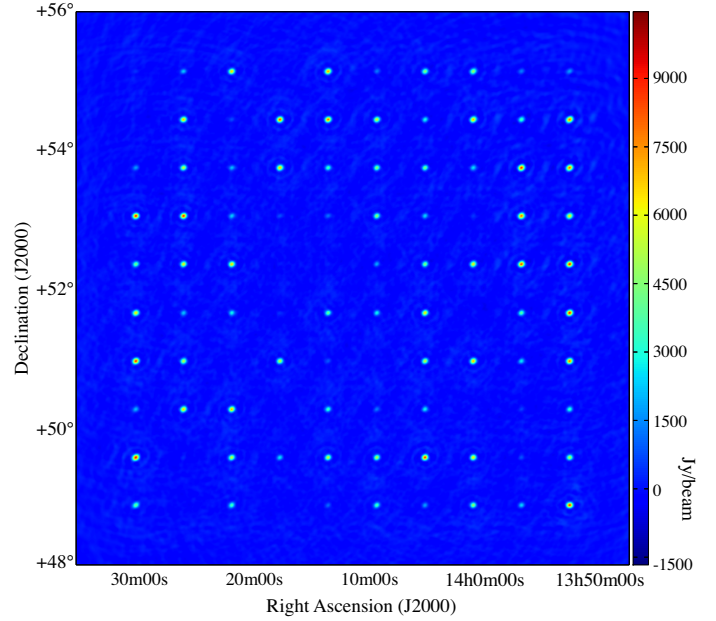


**Fig. 4.** Dirty image derived from a set of 100 simulated point sources with flux density ranging from 1 to 10000 Jy. Simulated visibilities are generated with dataset **B**. Some sources are not yet visible due to the high noise level.

the imaging, giving an effective angular resolution of  $\sim 3''$ . For CoSch-CLEAN, we used  $10^8$  iterations and for CS, we use 200 iterations. With CS, the sources are reconstructed with wavelets.

We report on figure 5, the output integrated flux density of all detected sources in the reconstructed images against the model flux densities of the model point sources. We again used pyBDSM to perform the source detection and characterization (including the 2D elliptical Gaussian fit of the source, position of the Gaussian barycenter, photometry along with the respective errors). The error bars of each point were obtained directly from the photometry and are negligible given the low level of the background noise. However, these error bars don't include the bias of poorly reconstructed sources. With a perfect reconstruction, all points should lie on the diagonal of slope 1.

The output flux densities of the sources were computed from the output Jy/beam map after multiplication by the CLEAN beam area given by  $\text{Beam Area} = (\pi ab) / (4 \ln 2 p^2)$  with a, b the major (resp. minor) axes of the CLEAN Beam and p, the pixel size in the same unit as a and b. The intensity (in Jy/pixel) is then integrated over a small circular region around each source. For the CS reconstructed image, the effective source size was reduced to a few pixels gathered in smaller patches around the sources (as compared to the CLEAN model only constituted of a collection of pixels). The flux is more efficiently gathered around the source position, resulting in an increase of all pixel size values in the CS maps (in Jy/beam).

The resulting source size was  $3.2' \times 3.7'$  (i.e. the dimension of the CLEAN beam) for CoSch-CLEAN and between  $\sim 30'' - 1'$  (1-2 pixels) for CS. This result corroborates that of the previous study. The super-resolution brings here a factor of 3 to 6 improvement of the source size as compared to the size of the CLEAN beam, using exactly the same dataset for the two methods.

The flux density r.m.s. error was derived from the residual maps and account for 3.6 Jy/beam Std-dev of CS and 1.7 Jy/beam for CoSch-CLEAN. The error bars are not reported on

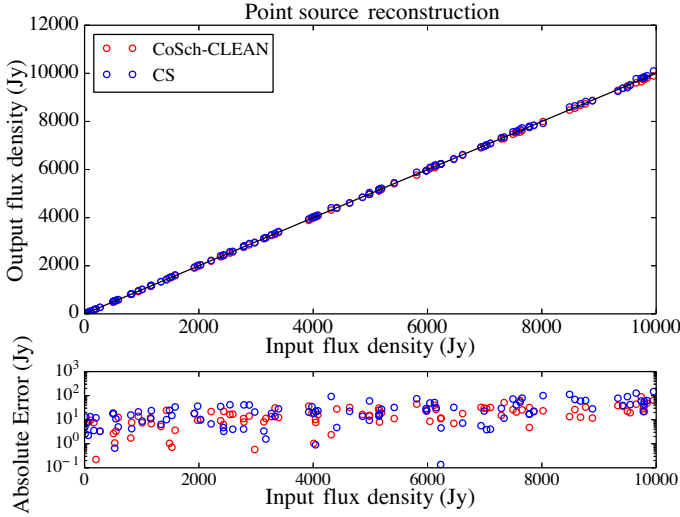


**Fig. 5.** (Top) Total flux density reconstruction for a set of point sources (Fig. 4) with original flux density spanning over 4 orders of magnitude with the original flux density (x-axis) vs. the recovered flux density (y-axis). The recovered flux densities for CoSch-CLEAN (red) and CS (blue) are represented on a linear scale whereas the absolute error is on a logarithmic scale for clarity. Perfect reconstruction lies along the black line (top) scatter plot of the absolute value of the error for each source. The output flux density values and errors are similar with both CoSch-CLEAN and CS.

the plot for clarity. The total flux density of the sources were recovered as shown by the distribution of points lying on the diagonal. The relative error (compared to the input flux density of each source) is not larger than 10% in most cases for both CoSch-CLEAN and CS. The flux density error is slightly increasing, with the source flux density as depicted by the scatter plot represented in a log-scale in Fig. 5 (bottom).

Due to the high number of strong sources, neither CoSch-CLEAN nor CS were able to reconstruct successfully some of the faintest sources that were barely above the background level. CoSch-CLEAN presents slightly greater performances for reconstructing correct flux densities with a lower error (the mean absolute error is 19 Jy for CLEAN and 29 Jy for CS, see Fig. 5). Nevertheless, CS led to the detection of more faint sources that were missed by CoSch-CLEAN, but with a larger error on their flux density values. In spite of its improved angular resolution and its detection capacity, CS produced a larger standard deviation (3.6 Jy/beam) on the residual image than CoSch-CLEAN (1.7 Jy/beam). This could be an effect of the thresholding taking place in CS or the choice of the dictionary which is not perfectly fitted to represent point sources.

We have not noticed any particular dependance with the radial distance from the phase center for both CoSch-CLEAN and CS. The astrometric error was significantly low for both CoSch-CLEAN and CS (i.e. the recovered sources are at their expected locations at the scale of the pixel size) with the radial distance from the phase center. Only a residual expansion (from 1 pixel to several pixels) of the source size in CS can be noticed at the border of the image. With a classical imager operating in the small field approximation, distortion and flux density error increase with radial distance. As expected from AWimager, we don't see any clear presence of this effect (apart from at the border of the field) with CoSch-CLEAN or CS. Within AWimager, the computation of the A- and W-projections dramatically reduce this error (Tasse et al. 2012).

During this study, CS performed similarly to CoSch-CLEAN with the same systematic errors on the reconstructed flux density (due to the large dynamic of the simulated sources). CLEAN-based algorithms stay highly competitive with CS in the scope of point source reconstruction but CS can be improved further. We know that the wavelet dictionary involved in the reconstruction of the sky with CS is not as efficient as a Dirac (or pixel) dictionary for representing single point sources. Future implementation of dictionaries will improve the handling of point sources.

### 3.3. Extended sources

We have shown that CS and CLEAN are clearly competing when imaging point sources. We now address the reconstruction of extended radio emission. Because these emissions are not strictly composed of point sources, the signal will be less sparse in a pixel dictionary, we therefore continue to use the wavelet dictionary, in order to ensure sparsity of the measured signal. We will first present the results with a simulation of W50 (§3.3.1) and then discuss the results of CS on a real LOFAR observation, that of Cygnus A (§3.3.2).

#### 3.3.1. A simulated observation: the W50 nebula

The W50 nebula (hosting the SS 433 microquasar) is an extended supernova remnant of large dimension ( $\sim 2^\circ \times \sim 1^\circ$ ) with internal filamentous structuring that makes it proper for benchmarking CS and CLEAN-based algorithms in an artificial situation. First, a test image for W50 was obtained from the final map of an original observation at 1.4 GHz carried out in Dubner et al. (1998) (Fig. 6 left). For the sake of this test, we intentionally used the higher frequency image of the source because of its higher density of structures at different spatial scales.

The radio map at 327.5 MHz was also available, but since it was imaged with the VLA in the D configuration, no structure smaller than  $70''$  was imaged. The angular resolution of the 1.4 GHz map is  $\sim 55''$ . We made the assumption that the higher spatial frequency features also emit in the LOFAR band (see W50 observed with LOFAR HBA in Broderick et al. (in prep.) and previous work). Part of the extraneous foreground and background features were removed to focus on the central extended feature only. We have set the flux scale of the model image to approximately match a total flux density of  $\sim 250$  Jy at 116 MHz (as interpolated from Fig. 3 in Dubner et al. (1998)). Second, we used the *predict* task included in AWimager to simulate the observed visibilities based on the input model image and on the input dataset **B**. We haven't manually inserted the artificial DDEs, as the purpose of this test is to monitor the reconstruction of the different types of algorithm. However, A-projection and W-projection were enabled for all runs. The hosting LOFAR dataset, in which the simulated visibilities of W50 were inserted, comes with a station layout providing a theoretical angular resolution of  $\sim 3''$ . This angular resolution is much lower than that given by the original image (for which the angular resolution is  $55''$ ). We therefore expect to have good results for CoSch-CLEAN, MS-CLEAN and CS. The *predict* step will naturally sample the image at the resolution accessible by LOFAR. Also, the instrumental and observational parameters of this generic dataset do not match with the real position of W50 in the sky. Given the extended size of W50, the dimensions of the simulated field are  $3.8^\circ \times 3.8^\circ$ . Third, artificial Gaussian noise was injected into the simulated visibilities. In the image, it generated a

resulting r.m.s. value equal to  $3 \times 10^{-4}$  of the peak of the dirty *noise-free* image (corresponding to a dynamic range of  $\sim 4000$ ).

Despite being in an unphysical situation, the resulting dataset will enable us to inspect the quality of the reconstruction using three methods: CoSch-CLEAN, MS-CLEAN and CS. The last two methods were implemented in *AWimager*: the MS-CLEAN method was imported from the *LWimager*, the standard LOFAR imager that corrects only for the W-projection (superseded by using *AWimager*), into which the CS method was also incorporated in addition to *AWimager* (see §3.1).

As we possess the input model image, we are able to track the effective angular resolution of the reconstructed images by inspecting the error image, and the convergence of the methods by inspecting the residual images. The primary imaging parameters are gathered in Table 2, which will also be the reference table for the imaging of Cygnus A.

We compare in Fig. 7, the reconstructed images given by CoSch-CLEAN (left column), MS-CLEAN (middle column) and CS (right column), produced from the same dataset. From top to bottom are presented the reconstructed image, the model, the residual image, and the error image. From these images several numerical measures were extracted and gathered in Table 3.

The total flux density of the model image is 230 Jy, whereas the total reconstructed flux density values over the source are 229.2 Jy, 229.4 Jy and 229.7 Jy respectively for CoSch-CLEAN, MS-CLEAN and CS. These values are extremely close to each other, validating that all three methods (including CS) conserve the total flux density. This is a basic requirement that any new imaging method should verify.

The three methods rendered the extended emissions with different levels of accuracy, and a particularly good image was produced from CoSch-CLEAN due to the very low level of noise in the data and the high number of iterations. The MS-CLEAN image presents a lower angular resolution despite taking into account the various scales of the image. Testing with other sets of scales, thresholds, and number of iterations, did not seem to improve the result and sometimes led to divergence (especially after  $\approx 200$  iterations). This potential divergence may be caused by an not adapted thresholding when the background residual level is reached at the end of the convergence, the algorithm then start to get signal from the background noise. We also used the multi-scale method of *LWimager* and we obtained similar poor results on this dataset. The implementation of MS-CLEAN in *AWimager* is still experimental and need to be more extensively validated. This method is known to bring an improved representation of extended sources. The restoring beam was  $2.8' \times 2.4'$  for CoSch-CLEAN and  $2.8' \times 3.3'$  for MS-CLEAN. The CS image is visually sharper than the other two and contains high frequency features that were recovered during the imaging. From the typical size of the few point sources included in the CS image, the effective angular resolution of the image was  $\sim 1' \times \sim 1'$ , representing almost a factor 2.5-3 improvement and nearly equal to the  $55''$  original resolution of the input model image.

The associated model images are, by construction, dependent on the method used for imaging. The CoSch-CLEAN presents the distribution of CLEAN components that are then convolved by the restoring beam to produce the reconstructed image. With MS-CLEAN, the extended features are represented in the model, along with some pixel-sized CLEAN components. As described earlier, the output of CS comes directly as the best estimation of the sky and is in units of Jy/pixel. We multiplied this map by the beam area to get a map in the same brightness units (Jy/beam) as the other maps. Therefore, the model image

and the reconstructed image only differs by the residual map that was added to the latter. As noticed earlier, CS tends to concentrate the flux of a point source around a region of the source (see §3.2.1), and the wavelet dictionary is able to represent the extended emission.

Any vestigial structure in the residual image shows a lower rate of convergence which can be due to an insufficient number of iterations (which is presently not the case for the CLEAN-based algorithms), or a limitation due to the imaging method itself. In our case, a CoSch-CLEAN image, supposed to be fitted to point sources rather than extended emission, presents a very good residual Std-dev level ( $4.1 \cdot 10^{-4}$  Jy/beam) as compared to that of MS-CLEAN ( $1.3 \cdot 10^{-2}$  Jy/beam) in the present situation. However, the CS residuals Std-dev level is slightly better ( $3.2 \cdot 10^{-4}$  Jy/beam) across the image.

The error images are computed in the last row of Fig. 7, as the difference of the reconstructed image (converted to Jy/pixel, knowing the beam area of the restoring beam) with the initial full resolution input image (also in Jy/pixel). The input image was not degraded by convolution to match a particular resolution. From the different error images, CS is visually the one that provides the fewest discrepancies compared to the input model image. The high resolution features of the latter were partly restored and preserved by the CS reconstruction. The CS algorithm provides the smallest mean square error value over the image ( $4.8 \cdot 10^{-5}$  Jy/pixel) which represents an improvement of a factor  $\sim 2$  as compared to the present CoSch-CLEAN and MS-CLEAN reconstructed images.

We simulated realistic extended radio emissions inside a mock dataset and, as has been discussed in the literature previously mentioned, we demonstrate the feasibility of reconstructing images in a way that is compatible within the current LOFAR system (using LOFAR data and imaging tools, and taking DDEs into account). The next step of our benchmarking is to apply our method to a *real* observation by using a real dataset taken with LOFAR. The next example focuses on the image reconstruction of the so-called *A-team* radiosources that have become well-known in radio interferometry.

### 3.3.2. A real LOFAR Observation: the Cygnus A radiogalaxy

Cygnus A (3C 405) is one of the most powerful radio galaxies that can be observed. It represents a good test case for benchmarking our method. It contains extended emission, originating from two main radio lobes separated by a distance of  $\sim 120$  kpc, representing a projected size of  $\sim 2' \times 1'$  on the sky. The energetic particles responsible for the emission in these radio lobes originate from jets coming from the central radio core. At the extremities of each lobe, are located compact sources (called hotspots A and B on the west lobe and hotspot D in the east lobe, as labelled in Hargrave & Ryle (1974)). Cyg A has recently been observed by LOFAR during its commissioning phase (McKean et al. 2010, 2011) but has also been observed in the past at low frequencies (see for example Lazio et al. (2006) and references therein, which observed Cygnus at 74 MHz and 327 MHz with the VLA). We have used a real calibrated dataset at  $\sim 151$  MHz (dataset C in Table 3.1) produced by the LOFAR instrument, which includes real measurements and noise contributions. The observation was performed in March 2013, then processed and finally calibrated on the ‘‘Perley-Butler 2010’’ absolute flux scale (refer to McKean et al. (2010, 2011) and references therein for past work on this radio source at these frequencies). Unlike W50, the Cygnus A dataset is consistent in terms of (noisy) data, as it

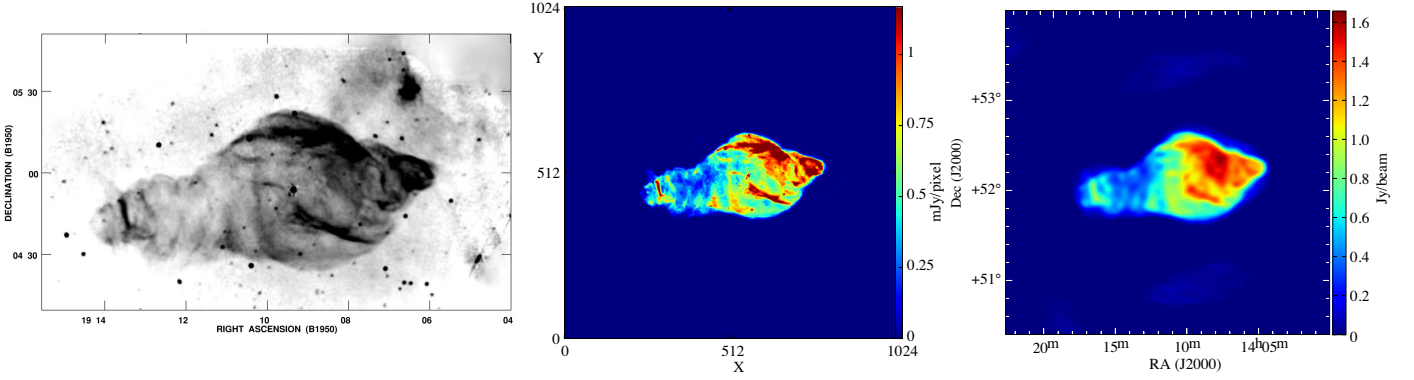


**Fig. 6.** (left) Original 1.4 GHz radio map from Dubner et al. (1998) (pixel size =  $6.75''$ , ang. resolution =  $55''$ ), (middle) prepared input model image scaled to the approximate total flux density of 230 Jy ( $1024 \times 1024$  with pixel size of  $13.5''$ ), and (right) the dirty image obtained with dataset **B**. All emission falling outside the extended emission of W50 was put to zero, however, point sources that are inside W50 were kept in the simulation.

Algorithm	W50			Cygnus A		
	CoSch-CLEAN	MS-CLEAN	CS	CoSch-CLEAN	MS-CLEAN	CS
specific parameter	–	5 scales	–	–	5 scales	–
weight	Briggs (robust = 1)			Uniform		
Planes for W-projection	11					
image size	$1024 \times 1024$			$512 \times 512$		
padding	1.6			1.5		
pixel size	$13.5''$			$1''$		
threshold	$10^{-3}$ Jy	$10^{-3}$ Jy	$10^{-3}$	0.5 Jy	0.5 Jy	0.5
gain	0.01	0.4	0.4	0.05	0.05	0.05
$N_{iter}$	$10^8$	$10^3$	200	$3 \cdot 10^4$	$10^4$	200

**Table 2.** List of relevant imaging parameters used by *AWimager* for CoSch-CLEAN, MS-CLEAN, and CS, for the two extended objects. For MS-CLEAN, we have used scales at [0,10,30,70,100] pixels for W50, and [0,2,5,10,15] pixels for Cygnus A.

corresponds to the real noise measured from the sky at the particular time/frequency integration of the observation.

As for W50, we have used *AWimager* with the three imaging methods, to image Cygnus A (the imaging parameters are gathered in table 2). With the FoV being relatively small, and the source being the dominant source in the dataset, the DDEs are expected to be low. In Fig. 8, we show a similar set of output images to that presented for the W50 simulations. However, we don't have an input model image with which to compute the error image. From the left to the right column are the reconstructed map with CoSch-CLEAN, MS-CLEAN and CS. The first row presents the constructed images in Jy/beam, the second row, the model images in Jy/pixel, and in the third row, the residuals. Meaningful quantities obtained from these images are shown in Table 3.

All the three imaging methods were able to render a proper image of the emission, given the extremely good quality of the data and its strong brightness. The CoSch-CLEAN image shows residual high frequency structures that lead to distortion of the source. These artifacts mainly come from CLEAN components collected from the noise background residual map. With our incorporation of MS-CLEAN in *AWimager*, we obtained a similar brightness distribution to that obtained in McKean et al. (2011). The restoring beam size was  $6.1'' \times 5.0''$  with both methods. The CS effective angular resolution is  $\sim 2.8'' \times 2.8''$ , representing again a factor of 2 improvement. The resulting CS image shows a similar overall brightness distribution but with a much sharper representation of the structure inside the lobes. In partic-

ular, the hotspots A, B and D were correctly imaged without any ambiguity as compared to the result obtained with both CoSch-CLEAN and MS-CLEAN. To check the correct representation of the features in the image, we show in Figure 9, an overlay of the CS image with VLA contours obtained at 327.5 MHz at a resolution of  $2.5''$ . The location of hotspots and features inside each radio lobe (filaments and holes) match that of the VLA map. This confirms the major improvement in the angular resolution brought about by CS.

The composition of the model images depends on the kind of method that was used to generate the image. Whereas the CoSch-CLEAN model image is only composed of pixel CLEAN component sources, which add up after convolution to form the image, MS-CLEAN displays a more smooth distribution of the source, based on the multi-scale approach. The CS (model) image is mainly dominated by the signal of the hotspots situated at each extremity of the lobes. Again, the reconstructed CS image represents the best approximation of the sky, making this map directly exploitable scientifically.

We can check the scientific relevance of the reconstructed images by inspecting different quantities (gathered in Table 3). The first quantity is the total integrated flux density of the source. This value can be measured with short-spacings (ideally with a 0-length baseline or with the autocorrelation of the antennas) or by fitting the variation of the visibility amplitude vs. the  $(u,v)$  radial distance and measuring the Y-intercept of this curve. In the present case, the observing frequency is 151 MHz and the total flux density is expected to be close to  $\gtrsim 10500$  Jy when looking

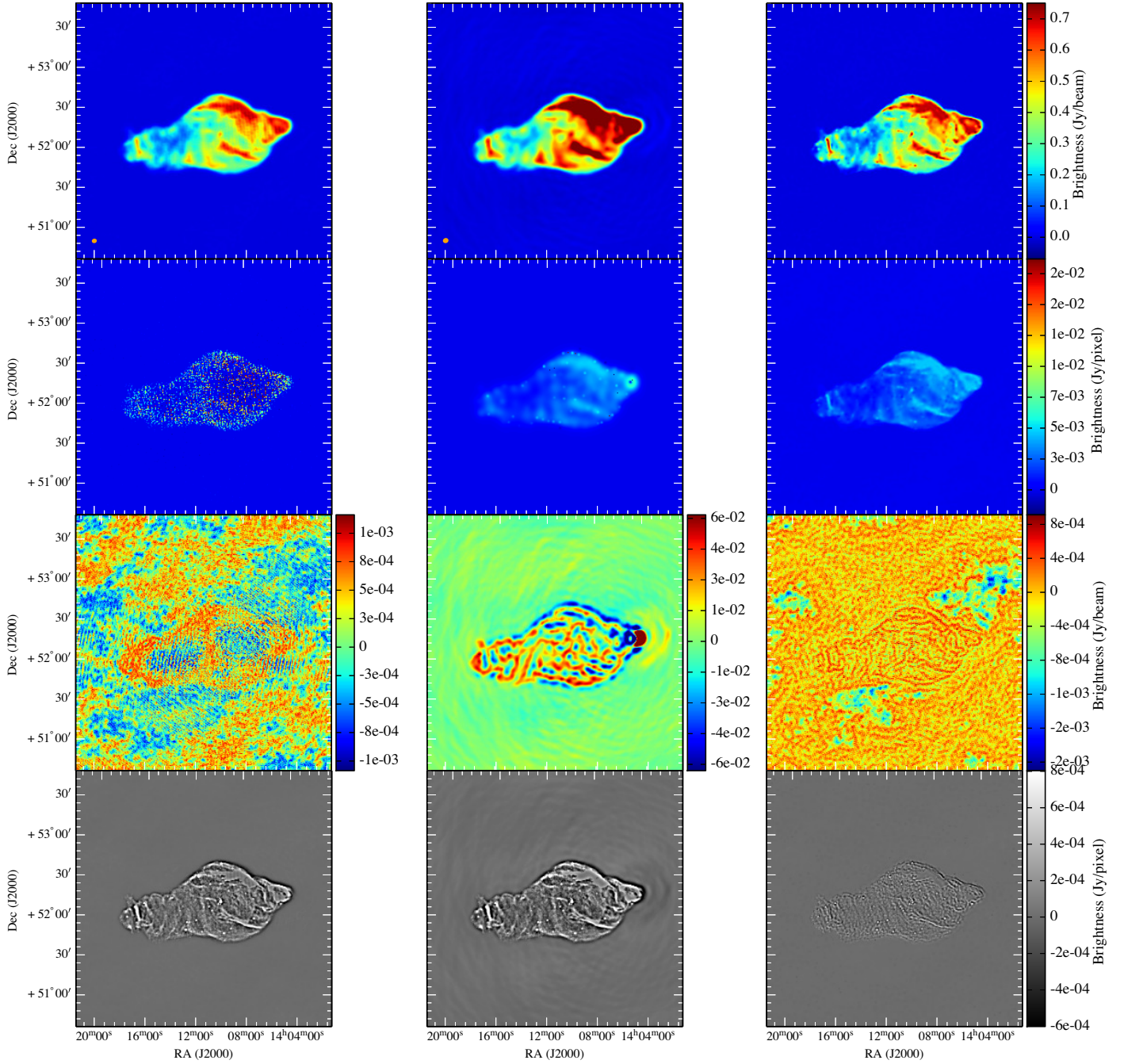


**Fig. 7.** Reconstructed images of W50 from the simulated LOFAR observation (dataset **B**) using CoSch-CLEAN (left column), MS-CLEAN (middle column), and CS (right column). From top to bottom are the restored image (in Jy/beam), the model (in Jy/pixel), and the residual and the error images. The CS restored and model images only differs by their scaling (the former is in Jy/beam using the beam area of the CoSch-CLEAN beam and latter is in Jy/pixel). The color scales of the images are different for each row, as indicated by the color bar on the right. The residual images are displayed with their respective color bar. The CS reconstruction contains high spatial frequency information restored from the dataset. The effective angular resolution of the CS image ( $50''$ ) is close to that of the original input image ( $55''$ ). In addition, the error image shows a larger proximity between CS and the original input image.

at the visibility data. A correct image reconstruction is therefore obtained when the total flux density present in the reconstructed image is close to that value. We derived, for each method, the total flux density of the source by summing the brightness (in Jy/beam) over one identical region containing all the main features, and multiplying it by the CLEAN beam area. We respectively find 10576 Jy, 10560 Jy and 10507 Jy for CoSch-CLEAN, MS-CLEAN, and CS. This range of total flux density is compatible with previous low-frequency observations taken at the same

frequency by MERLIN and LOFAR (Steenbrugge et al. 2010; McKean et al. 2011), within a 2% accuracy on the flux density. With this accuracy, we cannot conclude that one method is superior to another, however these values suggest that CS conserves the total flux (as seen for W50) similarly to the two other methods.

The residual images were represented on the same color scale. We measured the r.m.s level over the same region of flux integration and the standard deviation of the entire  $512 \times 512$

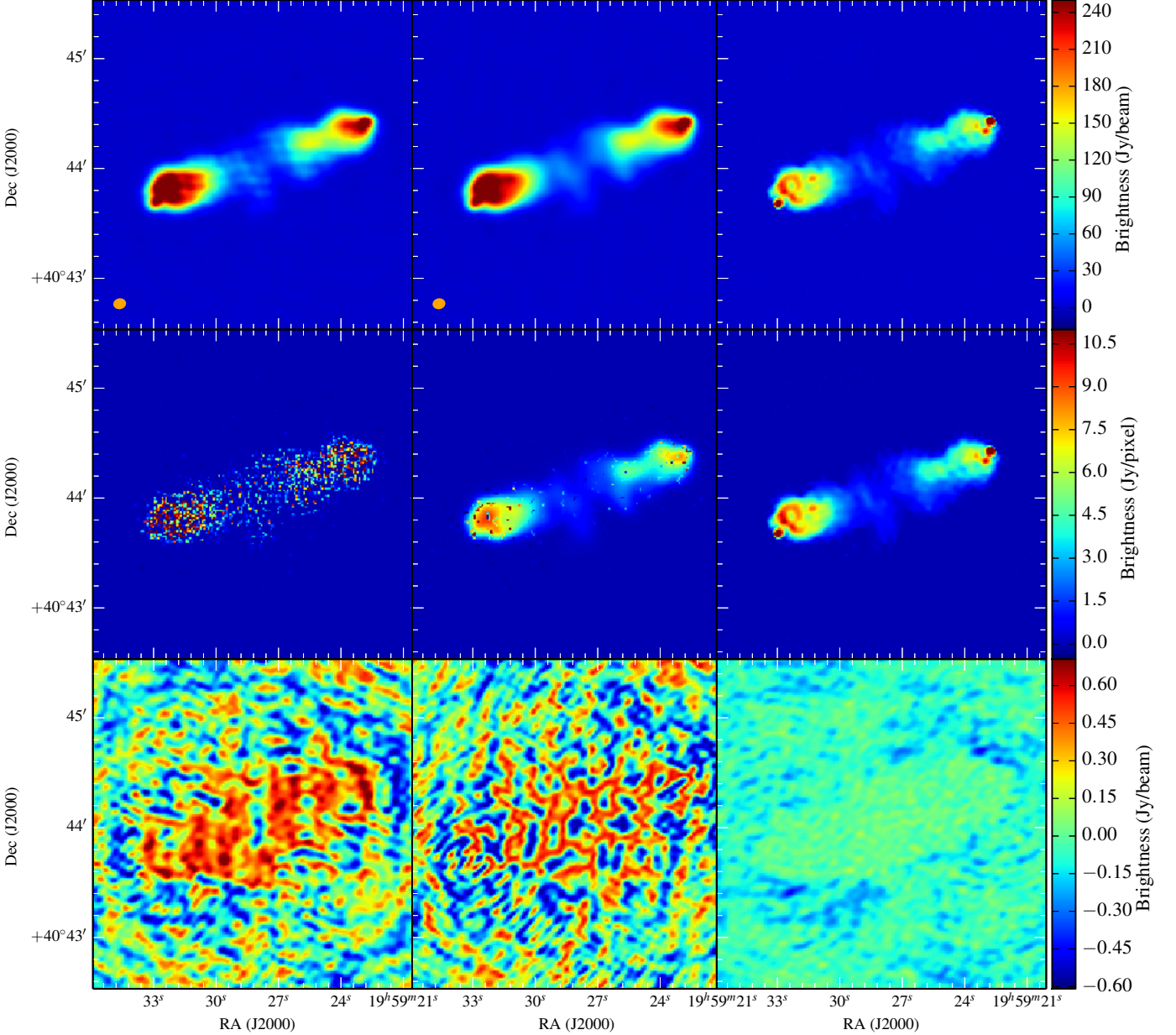


**Fig. 8.** Reconstructed images of Cygnus A from the real LOFAR observation (dataset C) using CoSch-CLEAN (left column), MS-CLEAN (middle column), and CS (right column). From top to bottom are the restored images, the model images and the residual images. There is no error image, as its calculation would require a highly resolved map of the true brightness distribution of Cygnus A to compare with the recovered image. The color scales of the images are different in each row, as indicated by the color bar on the right. The CS reconstruction presents a higher angular resolution and a lower residual level (see text) than that obtained with the two other methods.

residual map. The CS residuals show an improvement of about one order of magnitude than CoSch-CLEAN and MS-CLEAN. This result is characteristic of a reconstruction close to the real object.

The dynamic range (DR), computed as the ratio of the peak flux density to the residuals std-dev, was computed for each image. The DR are respectively 1799:1, 1619:1, and 8392:1, suggesting that CS enhances the DR of the image. This is achieved by the combination of two effects: first, CS tends to concentrate the flux in the data, at the correct astrometric position, resulting in a higher peak flux density of the image; second, the low standard deviation of the residuals demonstrates a better convergence of the image reconstruction. The DR of the MS-CLEAN

image is slightly lower than that of CoSch-CLEAN. This can be explained by the fact that the data are dominated by the source, making it easier to decompose in unambiguous CLEAN components, or by an unoptimized choice of the scale decomposition. Moreover, we inserted the MS-CLEAN method, already present in *LWimager*, inside *AWimager* so as to give a common framework to all the imaging methods. The discrepancies between the two methods may affect the quality of the reconstruction. In a more general scope, the DR is only limited by the reconstruction method itself (as already noticed for CLEAN in McKean et al. (2011)).

From the present results, it appeared that the CS method is robust enough to reconstruct extended radio emissions coming

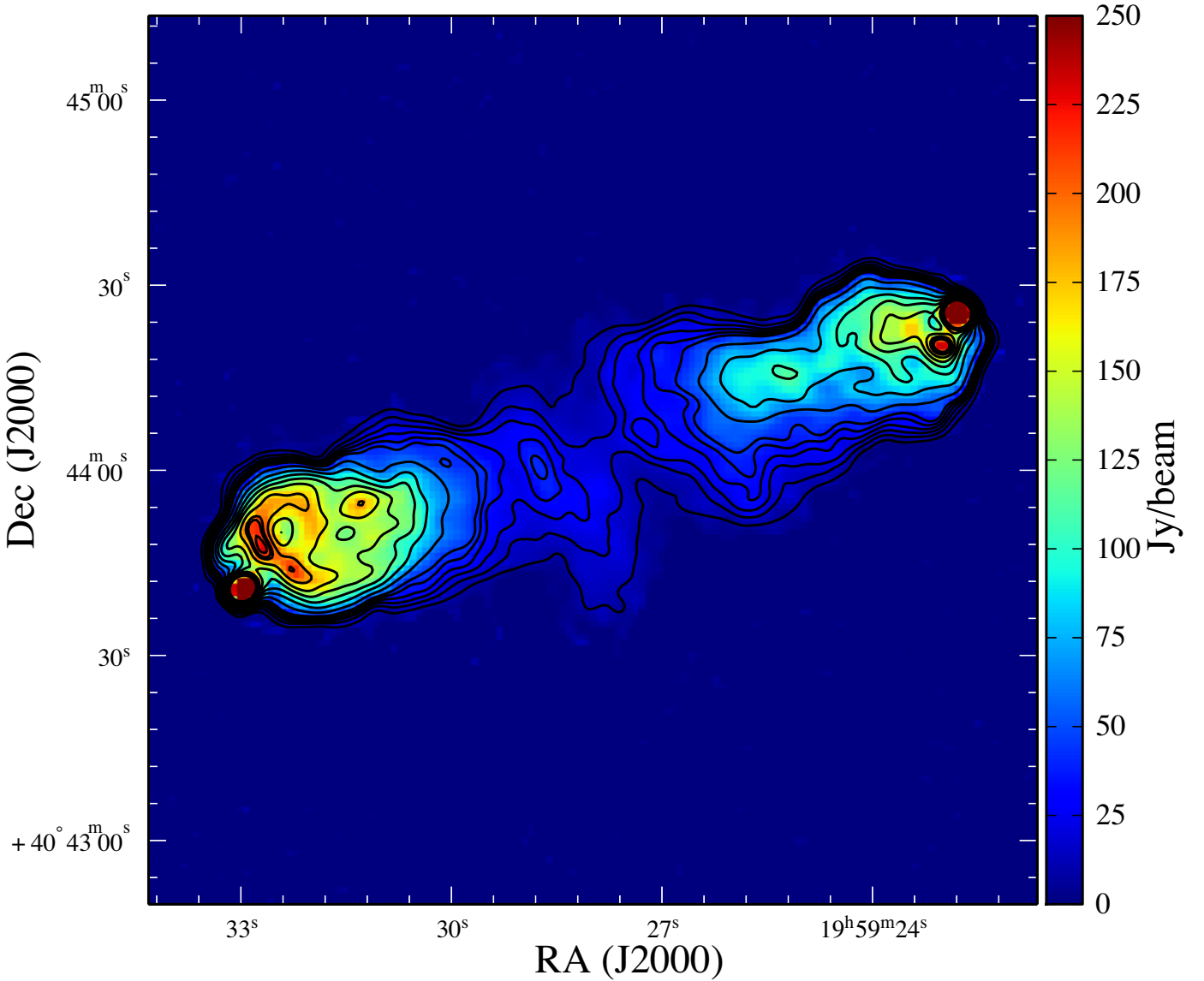


**Fig. 9.** Colorscale: reconstructed  $512 \times 512$  image of Cygnus A at 151 MHz (with resolution  $2.8''$  and a pixel size of  $1''$ ). Contours levels (Toggle contours) are [1,2,3,4,5,6,9,13,17,21,25,30,35,37,40] Jy/Beam from a 327.5 MHz Cyg A VLA image (Project AK570) at  $2.5''$  angular resolution and a pixel size of  $0.5''$ . Most of the recovered features in the CS image correspond to real structures observed at higher frequencies.

from simulated data as well as real LOFAR data. In the present situation, the high flux density of Cygnus A and the quality of its calibration contributed to quality of the CS reconstruction. We will pursue the study, for example by comparing the authenticity of recovered structures with those published science radio catalogues.

### 3.4. Summary of results

In this section, we benchmarked our implementation of CS against different types of data. The results from the reconstruction of unresolved sources (§3.2.1 & §3.2.2) and of extended sources (§3.3.1 & §3.3.2) are collected in Table 3.

CS has demonstrated the capability to perform as good as CLEAN with point sources, with a high astrometric and flux accuracy, and to be compatible with the DDEs framework and the LOFAR imaging tools. It also offers an alternative to multi-scale methods in the reconstruction of extended emission. An appropriate choice of signal representation and convergence con-

straints must be made, depending on the content and quality of the data (e.g. field of point sources, multi-component images, or a mix of both). These results may be improved in the future by the fine tuning of the CS parameters, the use of better-matched dictionaries, and the addition of new minimization algorithms (e.g. such as the reweighted L1 methods, presented in Candès et al. (2007), to remove the residual bias of the solution (Carrillo et al. 2013)).

## 4. Discussion

### 4.1. Instrumental limitations and final convolution

In the classical radio framework, the CLEAN algorithm produces a model map of the deconvolved sky, composed of CLEAN components existing within the pixel domain (with either positive or negative values). One of the final steps of the CLEAN algorithm is the convolution of this model map with a smooth function which is usually the elliptical Gaussian

<b>Point source (§3.2.1)</b>	<b>CoSch-CLEAN</b>	<b>CS</b>
Relative flux density error High SNR, Low SNR	3% – 23%	3% – 25%
Effective angular resolution	3.18'×2.55'	1.55'×1.09'
Astrometric error	<2'	<1'
<b>Grid of point sources (§3.2.2)</b>	<b>CoSch-CLEAN</b>	<b>CS</b>
Relative flux density error (Jy)	Fig. 4	
Residuals: Std-dev in <b>I</b> (Jy/beam)	1.7	3.6

<b>W50 (§3.3.1)</b>	<b>CoSch-CLEAN</b>	<b>MS-CLEAN</b>	<b>CS</b>
Effective angular resolution	2.8'×2.4'	2.8'×3.3'	~1'×~1'
Reconstructed: total flux density in <b>S</b> (Jy)	229.19	229.41	229.72
Reconstructed: Peak flux density in <b>I</b> (Jy/beam)	0.72	0.96	0.79
Residuals: r.m.s. in <b>S</b> (Jy/beam)	4.6.10 <sup>-4</sup>	2.71.10 <sup>-2</sup>	3.1.10 <sup>-4</sup>
Residuals: Std-dev in <b>I</b> (Jy/beam)	4.1.10 <sup>-4</sup>	1.3.10 <sup>-2</sup>	3.2.10 <sup>-4</sup>
Error: Mean Square error in <b>I</b> (Jy/pixel)	8.9.10 <sup>-5</sup>	1.0.10 <sup>-4</sup>	4.8.10 <sup>-5</sup>
DR	1729:1	75:1	2446:1
<b>Cygnus A (§3.3.2)</b>	<b>CoSch-CLEAN</b>	<b>MS-CLEAN</b>	<b>CS</b>
Effective angular resolution	6.1''×5.0''	6.1''×5.0''	2.8''×2.8''
Reconstructed: total flux density in <b>S</b> (Jy)	10576	10560	10506
Reconstructed: Peak flux density in <b>I</b> (Jy/beam)	315.5	309.3	465.7
Residuals: r.m.s. in <b>S</b> (Jy/beam)	0.37	0.35	0.09
Residuals: Std-dev in <b>I</b> (Jy/beam)	0.17	0.19	0.05
DR	1799:1	1619:1	8392:1

**Table 3.** Statistical results obtained from applying CoSch-CLEAN, MS-CLEAN, and CS to all the datasets **A**, **B** and **C**. The statistics are defined in the text and appear when applicable. **I** means that the quantity has been evaluated on the entire image, **S** in a defined region of the image (typically around the source).

fit of the center of the PSF (namely the CLEAN beam). Each detected point source (pixel) will therefore take the shape of the CLEAN beam, resulting in a voluntary degradation of the information included in the model map. Then, the residual map is added to produce the final image. In the classical radio imaging framework, this final convolution represents the expression of the natural resolution of the instrument, imposing a boundary on the size of the smallest “believable” feature in the image. Any structure that is smaller than the actual size of the CLEAN beam is therefore associated with artifacts emerging from the residuals. As demonstrated in the first benchmark experiment in §3.2.1, one can not use the CLEAN model image as an exploitable image because of the presence of the (positive or negative) CLEAN components at locations which do not correspond to that of real sources. The model image of CLEAN-based algorithms only has a sense when convoluted with the CLEAN beam. Any convolution with a smaller beam may result in the apparition of “unphysical” or distorted features in the image. The choice of the CLEAN beam also results from an aesthetic rendering of the final deconvolved image.

The sparse reconstruction with CS is based on a completely different paradigm. The output image is supposed to be (or at least close to) the *true* sky under certain conditions (see §2.4). We demonstrated that it was possible to break the natural angular resolution limitation imposed by the instrument in a low noise regime. Needless to say that the resulting CS *model* image does not have an infinite resolution, as it would require the reconstruction of a 2-D Fourier transform with an infinite support, and containing all spatial frequencies. Because we define the image size before the reconstruction, the size of the point source will be limited by the quality of the Fourier

reconstruction at high spatial frequencies, and the size of the image support. The equivalent “CLEAN” beam of the final CS image can be deduced from the size and shape of the point source, and preliminary studies suggest that this size may improve with number of iterations.

We chose not to convolve the final CS result with the CLEAN beam in order to preserved the recovered super-resolved features. As a consequence, the flux of the point sources is concentrated in smaller patches around the sources, resulting in higher pixel flux density values on Jy/beam maps obtained with CS (and scaled with the CLEAN beam area).

#### 4.2. Performance and convergence compared to CLEAN-based methods

CoSch-CLEAN and CS are iterative processes that execute similar operations at each iteration (MS-CLEAN only work on the image plane). An image, whether it contains point sources or extended emission, is transformed to visibilities using the  $A$  operator (see Eq. 2), and residual visibilities are transformed back to an image using  $A^T$ . Other different operations take place, for example, the deconvolution of the residual in the case of CoSch-CLEAN, and wavelet transforms and thresholding in the case of CS. However, the time taken to execute one elementary cycle is dominated by the  $A$  and  $A^T$  operators (containing the *gridding* and *degridding* steps to go from the visibilities data to the interpolated 2D Fourier plane and vice versa). Future implementations will include a major/minor cycle strategy, similar to CLEAN, to optimize the computation time by performing several loops in the image plane before going to the Fourier plane.

Without accounting for these steps that are specific to the imager (especially *AWimager*), a single iteration of CoSch-CLEAN and CS are performed in a comparable duration. For example, all things being equal, CoSch-CLEAN takes 1.88s to run one iteration on the W50 image where CS takes 1.76s.

The total number of iterations that CoSch-CLEAN and CS need to reconstruct an image from a LOFAR dataset depends on the observation, the imaging parameters used, and the convergence criterion. This number can vary by several order of magnitude in CoSch-CLEAN and MS-CLEAN, depending on the complexity of the sources in the data, whereas it is constant for CS because the latter always operates on the entire image during a single cycle. The number of iterations is closely linked to the gain value in the context of each algorithm. For CLEAN methods, increasing the value of the gain means a larger fraction of the PSF is removed at each iteration. This can lead to a faster convergence rate but also to a greater absolute level in the residuals. For CS, the gain ( $\mu$ , see Eq. 9) will similarly control the rate of consecutive updates of the residuals. For the current CS implementation, a rigorous convergence criteria has not yet been defined. The cycle stops either when a maximum number of iterations has been reached or if the improvement between two consecutive iterations falls below a predefined threshold  $\epsilon$  (Eq. 2). We set this number to 200, as derived from experimentation on different datasets. Future implementation will include the tracking of the convergence based on the residual r.m.s., and the determination of a robust stopping criterion.

CS performs well relatively to CLEAN in almost all situations. It was able to recover correctly the positions and the flux density of single point sources while bringing an improved angular resolution at high and moderate SNR regimes, breaking the limit imposed by the chosen CLEAN beam (or more widely by the instrumental PSF). In low SNR regimes ( $\text{SNR} \lesssim 5$ ), the angular separability of the CS applied to point sources falls back to that of CLEAN.

Both methods encountered difficulties with the lowest flux values, and the dynamic range might be improved by a correct fine tuning of the imaging parameters with the different methods. A more sophisticated way of studying point flux density recovery, would be to simulate many observations, each with a single point in the FoV, and at different random locations.

For extended sources, the question of source separability (§3.2.1) shifts to the question of the authenticity of the reconstructed features in terms of shape and flux density. The CS reconstruction of W50 produces an image that has more detailed features when compared to the CoSch-CLEAN and MS-CLEAN reconstructions. These extra recovered features are made accessible by the CS framework. CoSch-CLEAN does not give access, by construction, to this level of detail. Moreover, this method is more fitted to a sparse distribution of point sources rather than extended continuous sources; this is illustrated by the vestiges of the sources that remain in the error image and in the residuals. One has to remember that even if CoSch-CLEAN is limited when applied to extended emission, MS-CLEAN is still a very good alternative for reducing the image distortion due to the convolution of the CLEAN model image.

## 5. Conclusions and perspectives

### 5.1. Benchmark and future developments

The overall performance of CS, highlighted in this study, is very promising in the scope of LOFAR, and more generally in clas-

sical radio interferometry. We highlight three main major improvements brought about by CS.

First, the baseline performance of CS provides comparable reconstruction quality to that obtained with CLEAN-based imaging methods. In particular, it competes with CoSch-CLEAN in regards to the imaging of a high dynamic sky over a wide FoV filled with point sources.

Second, CS brings a higher angular resolution to the reconstructed map, as demonstrated by the point source separability (super resolution). This capability is robust in the presence of noise. The reconstructed features are associated with existing sources, and possess correct flux densities and low astrometric errors.

Third, CS was applied, on the one hand, to simulated extended emission with a realistic LOFAR dataset and, on the other hand, to a real calibrated dataset coming from a real LOFAR observation of Cygnus A. In both situations, the reconstruction obtained with CS was compatible with that obtained with the other methods. Starting with the same set of measured visibilities, CS was able to produce maps with greater angular resolution, demonstrating its ability to recover unsampled regions of the visibility function, thanks to the sparsity assumption made about the source. Those structures are realistic, and preserved by omitting a convolution with the CLEAN beam.

Finally, a lot of effort has been expended, from the beginning, on the integration of our code in the existing LOFAR tools, to make it compatible with direct and standard use within the scope of LOFAR. In particular, our current implementation of CS exists within *AWimager* (and *LWimager*), which is the standard LOFAR imager that can handle DDE (by performing both A- and W-projections). Throughout this study, we performed our tests on realistic LOFAR datasets (in the classical *Measurements Set* data format compatible with CASA (*Common Astronomy Software Applications*), one of the standard set of tools used for calibration and imaging (NRAO 2013).

The compressed sensing algorithm we have used – iterative soft thresholding – is not sophisticated, and other more sophisticated algorithms exist, e.g. SARA (Carrillo et al. 2012, 2013). There is much scope for modifying and experimenting with different minimization algorithms and their parameters, and this will be continued into the future and reported in future publications.

Reconstruction with a curvelet dictionary (Starck et al. 2003) is also possible in our implementation and leads, for the moment, to similar results. This specific dictionary further improve the sparsity of the solution when the source contains filamentous structures. The extensive use of this dictionary will be a subject of future CS investigation, and its application to radio interferometry. A complete study of the sensitivity of CS parameters variation, when applied to different sort of data, has not yet been done. Many tests led to an educated guessing of the value of each parameter. It appeared that the MAD estimation (Eq. 10) is particularly robust in the presence of a high level of noise, but produces similar results to fixed thresholding when the signal of the source is dominant in the data.

Performance improvements will be made to the computation of A, e.g. by using multithreading and GPGPUs (Hardy 2013). This will benefit both CoSch-CLEAN and compressed sensing. There is a possibility of splitting compressed sensing into a major and minor cycle, similarly to CoSch-CLEAN, which will improve its speed.

The previous results suggest that CS methods are now mature enough for wider applications involving real dataset coming from LOFAR, or other radio interferometers. To our knowl-

edge, considering other developments completed or in preparation, and those discussed in the literature, this is the first time that CS had been integrated into an existing imaging system, operating on real data produced by a current giant radiotelescope. In order to generalize it to other radio interferometers, we are now continuing this work by integrating our code to the standard imager of the CASA software package (*casapy*).

A complete validation of this code is also underway. In particular, we plan to study its robustness when applied to different visibility data sampling (i.e. sparse measurements brought by snapshot observations vs. non-sparse measurements of long time-integrated observations), different DDEs occurring with radio interferometers such as LOFAR (the effect of the element beam, polarization effects, ionosphere stability...), and toward various kind of resolved objects showing high dynamic range, and requiring different dictionaries (e.g. imaging of other complex and extended objects at low frequencies such as Virgo A, composed of a mix of extended emission and point sources). We also want to perform an extended scientific commissioning of the results obtained from the code used in various realistic situation (e.g. extended faint emission with low SNR, impact of the uv-coverage, performance on transient radio sources...)

Future applications of CS can be extended to multifrequency imaging and the imaging of transient sources that change during the course of an observation, and hence are imprinted only partially on the visibilities. CS must provide the capability to recover snapshot images from sparsely sampled uv-coverage data slices. Another aspect would be to investigate the use of CS for VLBI (*Very Long Baseline Interferometry*) imaging in LOFAR. By construction, an interferometer such as LOFAR presents a statistically lower number of very long baselines as compared to the high density of shorter baselines. The highest angular resolution of the image depends on the quality of the measurement performed at these baselines. The signal coming from the longest baselines is sparse by nature, noisy, and especially sullied with DDEs (e.g. the radio antennas are situated under different ionospheres). It is therefore of interest to find methods, such as CS, that can cope with the reconstruction of the true signal from these baselines.

The present time is devoted to the development of the next generation of radiotelescopes, such as SKA. The computational effort required to perform the observation, the data acquisition, distribution and processing, necessitates toward the development of hierarchical and distributed real-time processing. These developments rest on the success of the current SKA *pathfinders* and *precursors*<sup>4</sup>. In that scope, CS can also be applied to instrumental calibration of a small interferometer. As an example, the *Murchison Wide-field Array* (MWA) in Australia, has routinely deployed a fast imaging mode to perform real-time image plane calibration (Mitchell et al. 2008). Such a calibration mode, combined with CS methods that can approximate the content of the sky from very sparse measurements, can represent a major advance in instrumental calibration. The NenuFAR project (Zarka et al. 2012, in prep.) which is a stand-alone phased array interferometer formed from the extension of the French LOFAR station *FR606*, will have similar requirements. Moreover, this local interferometer offers a densely-filled uv-space with few long baselines ( $B_{\max} \sim 400$  m), and may benefit from CS reconstruction methods.

A larger community of astronomers (and especially imagers) is gathering around the emergence and the success of CS recon-

struction methods. In the scope of radio interferometry, a validation of these methods will establish CS as a new standard image reconstruction algorithm, complementary to CLEAN-based algorithms. The coming generation of radio instruments will be resource demanding and provide as many potential applications of CS.

## 5.2. Software availability

A stand-alone version of the CS software is available<sup>5</sup> for testing the CS code with different toy models. This package is called SASIR, for *Sparse Aperture Synthesis Interferometry Reconstruction*, and comes with its source code. It demonstrates the feasibility of the sparse reconstruction using either an original model image and a mask in FITS format (representing the (u,v) sampling of the instrument), or a complex FITS image coming from the data gridding of a given measurement set. The operator *A*, central to the experiments of this paper, is computed directly inside the *AWimager* and can not be extracted easily from the LOFAR framework, as it changes for every measurement set, and refers to specific LOFAR dependencies for the computation of the direction dependent effects (antenna beam, polarization, projection effects...). The access to the source code of *AWimager* can be obtained by contacting Cyril Tasse and colleagues (Tasse et al. 2013).

*Acknowledgements.* We acknowledge the financial support from the UnivEarthS Labex program of Sorbonne Paris Cité (ANR-10-LABX-0023 and ANR-11-IDEX-0005-02). LOFAR, the Low Frequency Array designed and constructed by ASTRON, has facilities in several countries, that are owned by various parties (each with their own funding sources), and that are collectively operated by the International LOFAR Telescope (ILT) foundation under a joint scientific policy. VLA data of 3C 405 comes from the online NRAO Archive (the National Radio Astronomy Observatory is a facility of the National Science Foundation operated under cooperative agreement by Associated Universities, Inc.).

## References

- Barbey, N., Sauvage, M., Starck, J.-L., Ottensamer, R., & Chaniel, P. 2011, *A&A*, 527, A102
- Beck, A. & Teboulle, M. 2009, *SIAM J. Img. Sci.*, 2, 183–202
- Begeman, K., Belikov, A. N., Boxhoorn, D. R., et al. 2011, *Future Gener. Comput. Syst.*, 27, 319
- Bhatnagar, S., Cornwell, T. J., Golap, K., & Uson, J. M. 2008a, *A&A*, 487, 419
- Bhatnagar, S., Cornwell, T. J., Golap, K., & Uson, J. M. 2008b, *A&A*, 487, 419
- Bobin, J., Starck, J.-L., & Ottensamer, R. 2008, *IEEE Journal of Selected Topics in Signal Processing*, 2, 718
- Broderick, J. W., Miller-Jones, J. C. A., & LOFAR builder's list, t. in prep.
- Candès, E., Romberg, J., & Tao, T. 2006, *Information Theory, IEEE Transactions on*, 52, 489
- Candès, E. J., Wakin, M. B., & Boyd, S. P. 2007, *Enhancing Sparsity by Reweighted  $\ell_1$  Minimization*
- Carrillo, R. E., McEwen, J. D., & Wiaux, Y. 2012, *MNRAS*, 426, 1223
- Carrillo, R. E., McEwen, J. D., & Wiaux, Y. 2013, *ArXiv e-prints*, originally published: New York : Wiley, 1983
- Clark, B. G. 1980, *A&A*, 89, 377
- Combettes, P. L. & Pesquet, J.-C. 2011, *Fixed-Point Algorithms for Inverse Problems in Science and Engineering* (Springer-Verlag), 185–212
- Cornwell, T. J. 2008, *IEEE Journal of Selected Topics in Signal Processing*, 2, 793
- Cornwell, T. J., Golap, K., & Bhatnagar, S. 2008, *IEEE Journal of Selected Topics in Signal Processing*, 2, 647
- Cornwell, T. J. & Perley, R. A. 1992, *A&A*, 261, 353
- de Bruyn, A. G. & LOFAR EoR Key Science Project Team. 2012, in *American Astronomical Society Meeting Abstracts*, Vol. 219, American Astronomical Society Meeting Abstracts #219, 214.05
- de Gasperin, F., Orrù, E., Murgia, M., et al. 2012, *A&A*, 547, A56
- Dewdney, P., Hall, P., Schilizzi, R., & Lazio, T. 2009, *Proceedings of the IEEE*, 97, 1482

<sup>4</sup> <https://www.skatelescope.org/technology/precursors-pathfinders-design-studies>

<sup>5</sup> <http://www.cosmostat.org/software.html>

- Donoho, D. 2006, *IEEE Transactions on Information Theory*, 52, 1289
- Dubner, G. M., Holdaway, M., Goss, W. M., & Mirabel, I. F. 1998, *AJ*, 116, 1842
- Fannjiang, C. 2013, *A&A*, 559, A73
- G.Davis, S.Mallat, & M.Avellaneda. 1997, *Journal of Constructive Approximation*, 13, 57–98
- Hamaker, J. P., Bregman, J. D., & Sault, R. J. 1996, *A&AS*, 117, 137
- Hardy, S. J. 2013, *A&A*, 557, A134
- Hargrave, P. J. & Ryle, M. 1974, *MNRAS*, 166, 305
- Heald, G. & LOFAR Collaboration. 2013, in *American Astronomical Society Meeting Abstracts*, Vol. 221, *American Astronomical Society Meeting Abstracts*, 215.07
- Högbom, J. A. 1974, *A&AS*, 15, 417
- Lannes, A., Anterrieu, E., & Marechal, P. 1997, *A&AS*, 123, 183
- Lazio, T. J. W., Cohen, A. S., Kassim, N. E., et al. 2006, *ApJ*, 642, L33
- Leonard, A., Dupé, F.-X., & Starck, J.-L. 2012, *A&A*, 539, A85
- Li, F., Brown, S., Cornwell, T. J., & de Hoog, F. 2011a, *A&A*, 531, A126
- Li, F., Cornwell, T. J., & de Hoog, F. 2011b, *A&A*, 528, A31
- Li, F., Cornwell, T. J., & de Hoog, F. 2011c, *A&A*, 528, A31
- McEwen, J. D. & Wiaux, Y. 2011, *MNRAS*, 413, 1318
- McKean, J., Ker, L., van Weeren, R. J., et al. 2011, *ArXiv e-prints*
- McKean, J., Ker, L., van Weeren, R. J., Batejat, F., & et al. 2010, in *10th European VLBI Network Symposium and EVN Users Meeting: VLBI and the New Generation of Radio Arrays*
- Mitchell, D. A., Greenhill, L. J., Wayth, R. B., et al. 2008, *IEEE Journal of Selected Topics in Signal Processing*, 2, 707
- NRAO. 2013, *CASA: Common Astronomy Software Applications*
- Pandey, V. N., van Zwieten, J. E., de Bruyn, A. G., & Nijboer, R. 2009, in *Astronomical Society of the Pacific Conference Series*, Vol. 407, *The Low-Frequency Radio Universe*, ed. D. J. Saikia, D. A. Green, Y. Gupta, & T. Venturi, 384
- Ramos, E. P. R. G., Vio, R., & Andreani, P. 2011, *A&A*, 528, A75
- Sault, R. J., Hamaker, J. P., & Bregman, J. D. 1996, *A&AS*, 117, 149
- Schwab, F. R. 1984, *AJ*, 89, 1076
- Shulevski, A. 2010, PhD thesis, Leiden University, the Netherlands
- Stappers, B. W., Hessels, J. W. T., Alexov, A., et al. 2011, *A&A*, 530, A80
- Starck, J. & Bijaoui, A. 1991, in *High Resolution Imaging by Interferometry (European Southern Observatory)*
- Starck, J.-L., Bijaoui, A., Lopez, B., & Perrier, C. 1994, *Astronomy and Astrophysics*, 283, 349–360
- Starck, J. L., Donoho, D. L., & Candès, E. J. 2003, *A&A*, 398, 785
- Starck, J.-L. & Murtagh, F. 2006, *Astronomical Image and Data Analysis (Springer)*, 2nd edn.
- Starck, J.-L., Murtagh, F., & Fadili, M. 2010, *Sparse Image and Signal Processing (Cambridge University Press)*
- Steenbrugge, K. C., Heywood, I., & Blundell, K. M. 2010, *Monthly Notices of the Royal Astronomical Society*, 401, 67
- Tasse, C., van der Tol, S., van Zwieten, J., van Diepen, G., & Bhatnagar, S. 2013, *A&A*, 553, A105
- Tasse, C., van Diepen, G., van der Tol, S., et al. 2012, *Comptes Rendus Physique*, 13, 28
- Tukey, John W. (John Wilder), ., Mosteller, Frederick, .-, & Hoaglin, David C. (David Caster), . 2000, *Understanding robust and exploratory data analysis / edited by David C. Hoaglin, Frederick Mosteller, John W. Tukey, wiley classics library ed edn. (New York ; Chichester : Wiley)*
- van Haarlem, M. P., Wise, M. W., Gunst, A. W., & et al. 2013, *A&A*, 556, A2
- Vũ, B. C. 2013, *Advances in Computational Mathematics*, 38, 667
- Wakker, B. & Schwarz, U. 1988, *Annual Reviews of Astronomy and Astrophysics*, 200, 312
- Wenger, S., Magnor, M., Pihlström, Y., Bhatnagar, S., & Rau, U. 2010, *PASP*, 122, 1367
- Wenger, S., Rau, U., & Magnor, M. 2013, *Astronomy and Computing*, 1, 40
- Wiaux, Y., Jacques, L., Puy, G., Scaife, A. M. M., & Vanderghenst, P. 2009, *MNRAS*, 395, 1733
- Wilson, T. L., Rohlf, K., & Hüttemeister, S. 2009, *Tools of Radio Astronomy (Springer-Verlag)*
- Yatawatta, S., de Bruyn, A. G., Brentjens, M. A., et al. 2013, *A&A*, 550, A136
- Zarka, P., Girard, J. N., Tagger, M., & Denis, L. 2012, in *SF2A-2012: Proceedings of the Annual meeting of the French Society of Astronomy and Astrophysics*, ed. S. Boissier, P. de Laverny, N. Nardetto, R. Samadi, D. Valls-Gabaud, & H. Wozniak, 687–694
- Zarka, P., Girard, J. N., Tagger, M., Denis, L., & NenuFAR collaboration. in prep.